International Journal of Coal Geology 307 (2025) 104827

Contents lists available at ScienceDirect

International Journal of Coal Geology

journal homepage: www.elsevier.com/locate/coal

Hydrocarbon generation potential and organic carbon enrichment in evaporitic lacustrine source rocks from the Qianjiang Formation, Jianghan Basin (Central China): An integrated geochemical-petrological investigation

Rongbin Yang [a,b,c], Qingyong Luo [a,b,c,*], Jiapeng Wu [d,e], Qixiang Huang [a,b,c], Man Lu [a,b,c], Wenxin Hu [a,b,c], Dandan Wang [a,b,c], Zhengyu Chen [f], Jinqi Qiao [a,b,c]

[a] Hainan Institute of China University of Petroleum (Beijing), Sanya 572025, China
[b] State Key Laboratory of Petroleum Resources and Engineering, China University of Petroleum (Beijing), Beijing 102249, China
[c] College of Geoscience, China University of Petroleum, Beijing 102249, China
[d] China National Logging Corporation, Beijing 100101, China
[e] China National Logging Corporation, Rm241,Block C, Lot A12, Huanghe North Street Shahe Town, Changping District, Beijing 102206, China
[f] State Key Laboratory of Heavy Oil Processing, Petroleum Molecular Engineering Center (PMEC), China University of Petroleum, Beijing 102249, China

ARTICLE INFO

Keywords:
Hypersaline lacustrine basin
Unconventional shale oil
Organic matter enrichment
Source rock
Hydrocarbon generation potential
Jianghan basin

ABSTRACT

Continental hypersaline lacustrine basins constitute critical repositories of unconventional shale oil resources, often hosting source rocks with primary exploration value. The hydrocarbon generation potential and organic matter accumulation within the Qianjiang Formation of Jianghan Basin, however, remain elucidated inadequately. This study targets the third member of the Qianjiang Formation (Eq^3) through systematic analysis of dolomitic shale sequences from the QYP1 directional well in Qianjiang Depression. A comprehensive analytical approach is employed, integrating programmed open-system pyrolysis, major and trace element geochemistry, biomarker analysis, and organic petrology. The multidisciplinary framework is utilized to evaluate sediment provenance, organic matter supply, paleoenvironmental reconstruction (including paleoclimate, redox condition, and paleosalinity) during the Eq^3 depositional period, and the thermal maturity of organic matter. Based on these influencing factors, the hydrocarbon generation potential and organic matter enrichment model for source rocks of the Eq^3 interval are assessed.

Results demonstrate that the organic-rich sediments of the Eq^3 shales in the Qianjiang Depression exhibit exceptional hydrocarbon potential, qualifying as prime targets for shale oil exploration. Key characteristics include elevated total organic carbon (TOC), elevated $S_1 + S_2$ values, and superior hydrogen index (HI). Primary source of organic matter is attributed to saline lacustrine algae, as evidenced by a strong linear correlation between liptinite and TOC content and high proportion of lamalginite. The analyzed organic matter exhibits thermal maturity levels ranging from immature to low-mature level. Organic matter enrichment in these evaporative lacustrine source rocks is controlled by a combination of factors, including paleoclimate, sediment supply, organic matter sources, and depositional conditions. Paleoclimate reconstructions indicate that the Eq^3 interval was deposited under cold and arid conditions, with low Ga/Rb, SiO_2 and high K_2O/Al_2O_3, $Al_2O_3 + K_2O + Na_2O$, accompanied by weak chemical weathering with minimal sediment recycling. Depositional environment demonstrates strongly reducing conditions and exceptional organic matter preservation, as indicated by low Pr/Ph ratios, exceptionally high Gamm/C_{30} ($\beta\alpha + \alpha\beta$) hopane indices, rominent extended tricyclic terpanes ratios (ETR) and widespread pyrite occurrence. Elevated gammacerane, β-carotane content, along with high Sr/Ba, B/Ga and DBT/P radios, suggest high paleosalinity. Water column stratification further enhanced paleoproductivity and provided optimal conditions for organic matter preservation. Hydrocarbon-generating organic matter is predominantly derived from aquatic algae and halotolerant bacteria, with negligible contributions from terrestrial higher plants. Laminated algal mats dominate the organic composition, indicating extensive

* Corresponding author at: Basin and Reservoir Research Center, College of Geosciences, China University of Petroleum, No. 18, Fuxue Road, Changping District, Beijing, China.
E-mail address: qingyong.luo@cup.edu.cn (Q. Luo).

https://doi.org/10.1016/j.coal.2025.104827
Received 29 March 2025; Received in revised form 26 May 2025; Accepted 14 June 2025
Available online 25 June 2025

preservation of algae. This study is designed to elucidate the mechanisms governing organic matter enrichment in evaporative lacustrine basins and provides a robust foundation for shale oil exploration in the Qianjiang Depression.

1. Introduction

Lacustrine basins manifesting hypersaline geochemical signatures demonstrate exceptional lithofacies heterogeneity, served as critical preservation mechanisms for source rock while concurrently enabling multi-provenance organic matter enrichment (de Souza et al., 2024; Doyle et al., 2022; González-Sampériz et al., 2008; Hubert et al., 2018; Luo et al., 2018; Qiao et al., 2023). Intra-salt shale sequences in saline lacustrine systems have gained global recognition as significant hydrocarbon reservoirs, with major discoveries frequently associated with evaporite-rich successions (Shi et al., 2024; Wang et al., 2023; Warren, 2006). Unique lithological configurations and diagenetic modifications within these saline rhythmites establish favorable geological conditions for hydrocarbon accumulation, typically forming hybrid conventional-unconventional reservoirs with substantial exploration potential (Colman et al., 2002; Kong et al., 2020; Nunn and Harris, 2007; Pilcher and Blumstein, 2007). The Jianghan Basin, a representative intracontinental saline lacustrine system in China, contains multiple stacked saline shale sequences within the Qianjiang Formation, recognized as strategic exploration targets (Ge et al., 2023; Huang and Hinnov, 2014).

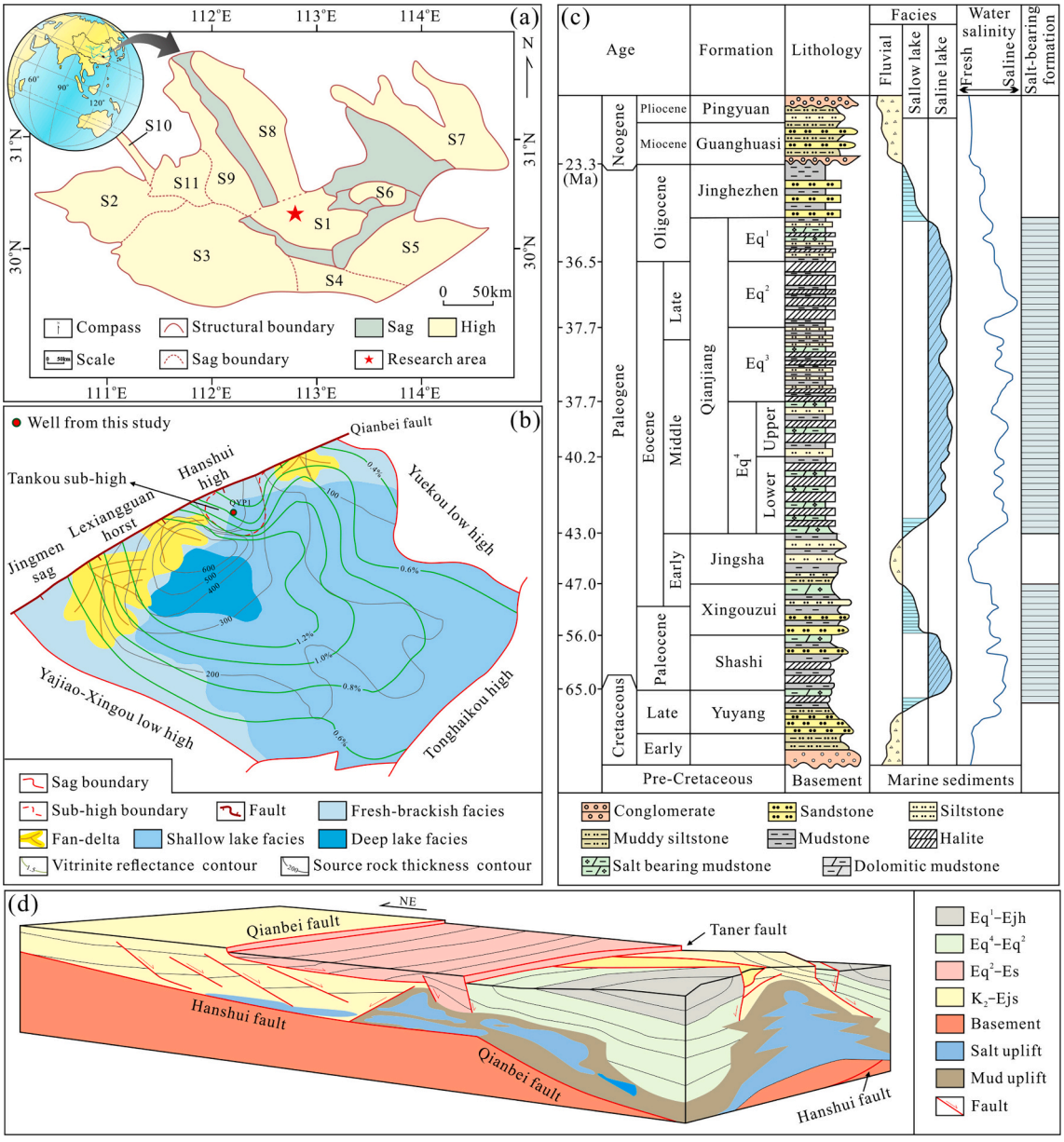

Fig. 1. (a) Geographical location of Jianghan Basin and distribution of tectonic units in the basin (Huang and Hinnov, 2014). (b) Distribution of adjacent tectonic units, sedimentary facies and the location of studied well (QYP1) in Qianjiang Depression (Huang and Hinnov, 2014). Isopach map of Eq^3 source rock thickness and vitrinite reflectance contour map of source rocks in the Qianjiang Sag are modified after Hou et al. (2017). (c) Lithostratigraphy, sedimentary facies, water salinity and the development of intersalt strata in Qianjiang Depression, Jianghan Basin (Huang and Hinnov, 2014). (d) Distribution of fault, plastic salt-mud diapirs and strata in Tankou area in the northwest margin of Qianjiang Depression (Gong et al., 2016).

Thick organic-rich black shales and dolomitic shales of the Qianjiang Formation exhibit premium source rock characteristics, including elevated organic matter abundance and superior hydrocarbon generation capacity (Hou et al., 2017). Systematic investigation of the Qianjiang Formation's geochemical properties and organic matter accumulation mechanisms provides critical insights for developing unconventional shale oil exploration strategies in evaporite-influenced lacustrine basins.

Sedimentary successions, particularly organic-enriched shale sequences, exhibit marked sensitivity to chemical weathering, depositional environment, and sediment recycling (Dera et al., 2009; Jarvie et al., 2007; Lu et al., 2025). Paleoclimatic forcings critically regulate weathering intensity and detrital sediment provenance, while simultaneously governing the biogeochemical proliferation of aquatic biota and terrestrial flora (Fedo et al., 1995; Nesbitt and Young, 1982; Qiao et al., 2023; Wu et al., 2024). Terrigenous clastic inputs exert profound controls on lithological assemblages and kerogen types, thereby modulating lacustrine depositional environment (Floyd and Leveridge, 1987; Kong et al., 2022; Taylor and McLennan, 1985). Additionally, the flourishing of aquatic organisms demonstrates strong covariation with paleosalinity and redox stratification patterns, collectively dictating hydrocarbon-generating organism sources and organic matter petroleum potential (Blumenberg et al., 2015; Lee et al., 2019; Luo et al., 2018; Romero-Viana et al., 2012; Volkman et al., 2015). As pivotal shale oil source units, the thermal maturation level and hydrocarbon generation potential of organic matter directly govern the quality and reserves of shale oil resources (Köster et al., 1997; Peakman et al., 1989; Mackenzie et al., 1980; Suárez-Ruiz et al., 2012). Previous studies on the Qianjiang Depression have primarily focused on the sequence stratigraphic framework, paleoclimatic variability, organic matter provenances, sedimentary environments, and shale oil resource potential within the Qianjiang Formation (Ge et al., 2023; Hou et al., 2017; Huang and Hinnov, 2014; Kong et al., 2022; Kong et al., 2020). The thrid member of Qianjiang Formation (Eq^3) has been characterized as a carbonate-enriched shale succession demonstrating hydrocarbon generation potential Nevertheless, a holistic synthesis integrating paleoclimate, depositional system dynamics, sediment provenance, and hydrocarbon precursor supply remains underdeveloped. Crucially, the degree of weathering-denudation processes affecting Qianjiang Formation sediments, in conjunction with the authigenic nature of organic components, constitutes a critical gap requiring systematic interrogation through integrated sedimentological and geochemical approaches.

This study employs an approach integrating organic geochemistry, elemental geochemistry, and organic petrology. The research aims to achieve the following objectives: (1) evaluate the thermal maturity and hydrocarbon generation potential of organic matter in the Eq^3, in the Tankou area, to assess its viability as an unconventional shale oil reservoir, (2) quantitatively characterize key factors, including paleoclimate, weathering intensity, redox conditions, and paleosalinity and hydrocarbon-generating organic matter supply, to identify the principal factors governing organic matter enrichment, and (3) systematically analyze the controlling factors of organic-rich sediments, ultimately formulating a predictive organic matter enrichment model for the Eq^3. This conceptual model will elucidate fundamental mechanisms governing organic matter accumulation in the evaporite-associated lacustrine system.

2. Geological setting

The Jianghan Basin, located in the middle reaches of the Yangtze River in central China, is a Cretaceous-Oligocene continental rift basin superimposed on Precambrian to Mesozoic basements (Huang and Hinnov, 2014; Fig. 1a). Its geotectonic framework is constrained by four orogenic belts: Qinling (northern margin), Dabie (eastern boundary), Jiangnan-Xuefeng (southern periphery), and Huangling Uplift (western limit). These elevated terrains act as predominant provenance for substantial clastic constituents within the basin, thereby exerting profound controls on the stratigraphic architecture through coupled mechanisms influencing both depositional assemblages and the tectonic configuration governing paleogeographic development (Castro et al., 2023; Khan et al., 2023; Morton et al., 2024; Walczak and Belka, 2017).

Evolved through multiphase tectonic reactivation and extensive sedimentary infill, 11 depressions and 4 uplifts have formed in the Jianghan Basin in 65 Ma years. Among these, the Qianjiang Depression emerges as hydrocarbon productive depressions (Grice et al., 1998). Situated in the central part of the basin, the Qianjiang Depression exhibits a distinctive lithological assemblage characterized by well-developed intra-salt shale sequences juxtaposed against a marked absence of regionally extensive halite-dominated evaporitic units. The particular evaporitic succession demonstrates progressive facies transitions from alluvial-lacustrine depositional systems to heterogeneous shallow brackish-profundal hypersaline lacustrine complexes, where in syndepositional halokinesis has fundamentally reworked the original evaporite distribution patterns (Grice et al., 1998; Philp et al., 1989; Fig. 1b). The depression's northwestern margin is demarcated by the Qianbei Fault, a crustal-scale discontinuity that modulated differential subsidence patterns under regional stretching stress during the middle Yanshanian to early Himalayan period (Dai, 1997; Gong et al., 2016). This fault system controls differential sedimentation rates on either side of the depression, facilitating in a thick sequence of source rocks and a well-defined depositional center on the footwall side during the Eq^3 sedimentary period (Dai, 1997; Huang and Hinnov, 2019). Notably, the Qianjiang Depression contains multiple sub-level hydrocarbon-generating sags, with the Banghu Sag being a prominent example (Ge et al., 2023; Pu et al., 2002). The Qianjiang Formation, representing a major phase of high-salinity lacustrine deposition, is characterized by diverse intersalt sequences with a sedimentary cover up to 4700 m in thickness and halite deposits reaching 1800 m thick (Huang and Hinnov, 2014). Studies indicate that the 193 rhythmic layers within the Paleogene Qianjiang Formation exhibit significant shale oil exploration potential (Hanson et al., 2001; Hou et al., 2017; Kong et al., 2022; Fig. 1c), which are conducive to preserving high-quality organic matter in the source rocks.

The Tankou sub-high, located adjacent to the Banghu-Wangchang hydrocarbon-generating center in the southeast domain, distinctive unique attributes shaped by tectonic-sedimentary coupling. This paleogeomorphic feature originated as a sequence of subaqueous paleo-uplifts governed by syndepositional stress adjustments and sediment dispersal dynamics. Structural control is prominently manifested along the Qianbei Fault zone, where thrusting and denudation have exposed plastic mudstone and salt layers (Fig. 1d). These layers, exhibiting fluid-like behavior, were compressed under stress to form diapiric structures, a distinctive feature of the region. A combined effects of the Qianbei Fault and the plastic salt-mud diapirs have created a well-defined slope belt within the Tankou area. This slope belt features a gentle upper section, a steep middle section, and a gradual transition to the depression at its base. Such a configuration has played a critical role in controlling the distribution and rhythmic deposition of the Qianjiang Formation (Gong et al., 2016).

3. Samples and methodology

3.1. Sample and preparation

Fifteen representative drill core specimens were systematically acquired from the QYP1 exploration well, strategically positioned within the Tankou structural salient along the northwestern periphery of the Qianjiang Depression in the Jianghan Basin (Fig. 1b). This directional well was specifically engineered for targeted sampling of a dolomitic mudstone reservoir interval within the Eq^3. Core specimens were sectioned into geometrically standardized rock blocks (12–14 mm width) perpendicular to bedding planes. Sequential preparation

involved solidification with epoxy resin followed by progressive polishing over a 24-h cycle to produce high-quality polished sections (with diameter of 25 mm and thickness ranging from 0.5 to 1 mm) ensuring optimal conditions for detailed microscopic analysis. Additionally, a set of 15 samples underwent mechanical pulverization using a tungsten carbide ball mill, with subsequent micronization to ≤200 mesh particle size distribution via quartz mortar grinding to ensure analytical-grade sample homogeneity.

3.2. Experimental analysis method

Experimental analyses were conducted at two specialized laboratories. Elemental analysis was performed at the Institute of Geochemistry, Chinese Academy of Sciences, while the remaining experiments administered at the State Key Laboratory of Petroleum Resources and Engineering, China University of Petroleum (Beijing).

3.2.1. Total organic carbon and programmed open-system pyrolysis

Total organic carbon (TOC) content was measured using a Leco CS230 carbon analyzer. Programmed open-system pyrolysis was performed using an OGE-VI oil and gas evaluation workstation. Powdered samples were analyzed with a flame ionization detector (FID) following a predefined temperature program to quantify hydrocarbon content. The temperature corresponding to the maximum S_2 peak (T_{max}) was recorded. Additionally, the hydrogen index (HI = S_2/TOC, in mg HC/g TOC) and oxygen index (OI = S_3/TOC, in mg CO_2/g TOC) were calculated to assess the quality and thermal maturity of the organic matter. For further methodological details, refer to Qiao et al. (2024).

3.2.2. Organic petrology

Organic petrological analyses were performed on 15 rock polished sections using a Leica DM4500P microscope equipped with a CRAIC microscope photometer. Photomicrographs were captured at 500 × magnification (50 × oil immersion objective) under ultraviolet (UV) fluorescence irradiation and reflected white light (halogen) using DISKUS Fossil software. Vitrinite reflectance (R_o) and observation of maceral were measured using a microscope photometer (MV-SP) at a wavelength of 546 nm. In accordance with ISO 7404-5, 2009, at least 50 valid vitrinite particles were carefully identified and measured for each sample to ensure the statistical reliability of the R_o measurements. The maceral composition of the Eq^3 samples from the Qianjiang Depression was established following the classification standards established by the International Committee for Coal and Organic Petrology (Gonçalves et al., 2024; International Committee for Coal and Organic Petrology (ICCP), 1998; Liu et al., 2018; Pickel et al., 2017). To ensure precision and representativeness, a systematic point-counting method was employed. For each polished section, a total of 3200 counting points were established, with a minimum requirement of 2800 effective points to achieve accurate quantification. This rigorous approach ensures statistically robust results that reflect the overall maceral composition of the samples. The integration of advanced microscopy techniques, standardized protocols, and meticulous point-counting methods provides a comprehensive understanding of the organic petrological characteristics of the studied samples.

3.2.3. Element analysis

In this study, the concentrations of major and trace elements in the samples were determined using an Agilent 720 ICP-OES (inductively coupled plasma optical emission spectrometry) and a Bruker Aurora M90 ICP-MS (inductively coupled plasma mass spectrometry), respectively. For detailed experimental conditions and procedures, refer to Qiao et al. (2025).

The enrichment factor (EF) of an element was used to evaluate its depletion or enrichment relative to a standard reference material (Tribovillard et al., 2006). The EF is calculated as follows:

$$X_{EF} = (X/Al)_{sample} \Big/ (X/Al)_{PAAS} \quad (1)$$

X represents the target element, and PAAS refers to the Post-Archean Average Australian Shale (Taylor and McLennan, 1985).

Nesbitt and Young (1982) proposed the use of the Chemical Index of Alteration (CIA) to assess the degree of weathering in the source area. Additionally, the Al_2O_3-CaO* + Na_2O-K_2O (A-CN-K) ternary diagram, Plagioclase Index of Alteration (PIA) and Weathering Index of Parker (WIP) were utilized to infer climatic and weathering conditions (Fedo et al., 1995; Parker, 1970). The CIA, PIA and WIP are calculated using the following formulas:

$$CIA = Al_2O_3/(Al_2O_3 + CaO^* + Na_2O + K_2O) \times 100 \quad (2)$$

$$PIA = (Al_2O_3 - K_2O)/(Al_2O_3 + CaO^* + Na_2O - K_2O) \times 100 \quad (3)$$

$$WIP = 100 \times (CaO/0.7 + 2 \times Na_2O/0.35 + 2 \times K_2O/0.25 + MgO/0.9) \quad (4)$$

It is imperative to concurrently perform the determination of the Index of Compositional Variability (ICV) to first to assess compositional maturity in order to constrain the calculation results of the CIA (Cox et al., 1995). The computational formula for ICV as follow:

$$ICV = (Fe_2O_3 + K_2O + Na_2O + CaO^* + MgO + TiO_2)/Al_2O_3 \quad (5)$$

In these formulas, the oxides are expressed in molar units. For the CIA, PIA, and WIP calculations, CaO* represents the CaO content in silicate minerals, excluding CaO from non-silicate minerals (e.g.,

Table 1
TOC and Rock-Eval pyrolysis of hypersaline dolomitic shale samples from Eq^3, the thrid member of Qianjiang Formation in Qianjiang Depression, Jianghan Basin, China.

Sample ID	Depth (m)	TOC (%)	S_1 (mg HC/g rock)	S_2 (mg HC/g rock)	S_3 (mg CO_2/g rock)	T_{max} (°C)	$S_1 + S_2$ (mg HC/g rock)	HI (mg HC/g TOC)	OI (mg CO_2/g TOC)
Q1–1	1596.2	6.82	6.82	41.97	0.88	432	48.79	615	13
Q1–2	1597.1	6.01	9.87	32.84	0.25	438	42.71	546	4
Q1–3	1600.4	0.85	2.66	4.80	0.57	423	7.46	563	67
Q1–4	1929.2	3.97	3.60	20.03	1.03	435	23.63	505	26
Q1–5	1934.3	6.91	3.15	27.97	0.26	437	31.12	405	4
Q1–6	1940.9	4.97	3.37	27.19	2.76	432	30.56	547	56
Q1–7	1944.5	0.84	1.68	4.97	0.88	425	6.65	592	105
Q1–8	2465.9	5.20	2.80	12.45	0.88	431	15.25	240	17
Q1–9	2581.3	0.55	2.42	4.18	0.65	428	6.60	760	118
Q1–10	2606.1	0.27	1.38	1.43	0.74	420	2.81	530	274
Q1–11	2609.2	0.52	2.59	3.09	0.69	430	5.68	594	133
Q1–12	2650.4	0.17	0.31	0.45	0.85	421	0.76	265	500
Q1–13	2654.60	0.23	1.29	0.77	0.72	418	2.06	335	313
Q1–14	2660.00	0.16	0.78	0.69	0.91	420	1.47	431	569
Q1–15	2661.00	0.44	2.23	1.86	0.67	433	4.09	423	152

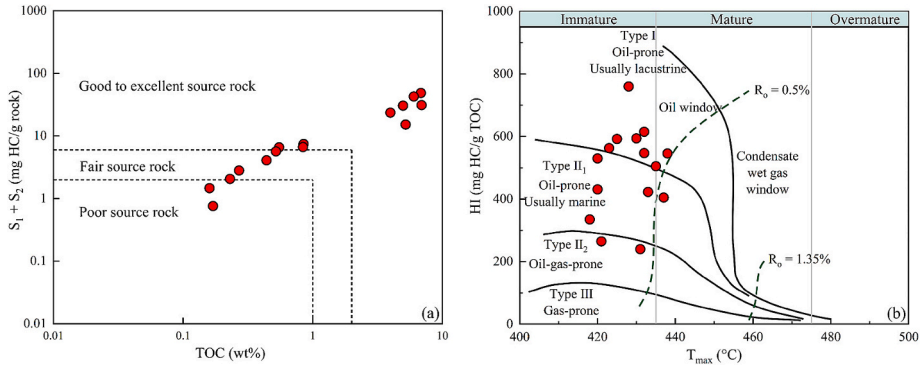

Fig. 2. Diagrams of (a) TOC versus $S_1 + S_2$, showing good quality source rocks in dolomitic shale samples. (b) T_{max} versus HI, showing thermal maturity of the Eq^3 samples in Tankou area.

carbonates and phosphates). McLennan (1993) proposed an indirect method to estimate CaO* by subtracting the CaO contribution from non-silicate minerals:

$$CaO^* = CaO - 10/3 \times P_2O_5 \quad (6)$$

In cases where the calculated CaO* exceeds Na_2O, the Na_2O content is used instead of CaO*. If CaO* is less than Na_2O, the calculated CaO* value is directly applied.

3.2.4. Gas chromatography-mass spectrometer (GC–MS)

Approximately 100 mg of powdered sample was subjected to Soxhlet extraction with dichloromethane for 72 h to isolate bitumen from the rocks. The extracted bitumen was subsequently fractionated into four components—saturated hydrocarbons, aromatic hydrocarbons, non-hydrocarbons, and asphaltenes—using a silica gel-alumina column and solvents of varying compositions and polarities. The relative abundances of these fractions were quantified for further geochemical analysis.

GC–MS analysis was conducted using an Agilent 7890-5975c system equipped with an HP-5MS fused silica column (60 m × 0.25 mm × 0.25 μm). High-purity helium (99.99 %) served as the carrier gas at a constant flow rate of 1 mL/min, with an ionization energy of 70 eV. For saturated hydrocarbons, the temperature program began with an initial hold at 50 °C for 1 min, followed by a ramp to 120 °C at 20 °C/min, then to 310 °C at 3 °C/min, and a final hold at 310 °C for 25 min. For aromatic hydrocarbons, the program started at 80 °C for 1 min, increased to 300 °C at 3 °C/min, and was maintained at 310 °C for 25 min. The injector temperature was set to 300 °C. The mass spectrometer scanned ion fragments within a range of *m/z* 50–550.

4. Results

4.1. Geochemical characteristics

The geochemical characteristics of the dolomitic shale samples from the Eq^3 exhibit significant variability along the vertical profile. TOC content ranges from 0.16 % to 6.91 %, with an average of 2.53 % (Table 1). Programmed open-system pyrolysis data reveal that the S_1 (free hydrocarbons), S_2 (residual hydrocarbons from kerogen pyrolysis), and S_3 (carbon dioxide from organic matter pyrolysis) values span 0.31–9.87 mg HC/g rock (average = 3.00 mg HC/g rock), 0.45–41.97 mg HC/g rock (average = 12.31 mg HC/g rock), and 0.25–2.76 mg HC/g rock (average = 0.85 mg CO_2/g rock), respectively (Table 1). The elevated S_1 and S_2 values, consistent with the high TOC content, indicate substantial hydrocarbon generation potential. The $S_1 + S_2$ ranges from 0.76 to 48.79 mg HC/g rock, with an average of 15.31 mg HC/g rock. The HI and OI vary from 240 to 760 mg HC/g TOC (average = 490 mg HC/g TOC) and from 4 to 569 mg CO_2/g TOC (average = 157 mg CO_2/g TOC), respectively (Table 1). T_{max} values, which reflect thermal maturity, are relatively low, ranging from 418 to 438 °C (average = 428 °C). The scatter plot of HI versus T_{max} provides critical insights into the thermal evolution of the organic matter (Fig. 2b).

4.2. Major and trace element

The major element composition of the QYP1 samples is summarized in Table 2. Relative to the PAAS, the Eq^3 samples show significant depletion in SiO_2, Al_2O_3, Fe_2O_3, and MnO. In contrast, CaO, MgO, and Na_2O exhibit relative enrichment. Notably, in some samples, the concentrations of CaO and MgO exceed those of SiO_2, while Na_2O levels consistently surpass 7 %. This compositional variability highlights the heterogeneous nature of terrigenous inputs and the diverse depositional conditions during the Eq^3 sedimentary period.

The K_2O/Al_2O_3 ratio ranges from 0.22 to 0.40 (average = 0.30) (Fig. 3b), while the P/Ti ratio varies between 0.39 and 2.74 (average = 0.92) (Fig. 10d). Elevated CaO and MgO concentrations suggest the presence of significant residual carbonate minerals. To account for this, Na_2O ratio is employed as a proxy for CaO*. Notably, the sample from 1944.5 m exhibits anomalously high Na_2O content, indicative of halite enrichment. CIA, PIA, WIP and ICV values range from 19.03 to 61.65 (average = 48.93), from 15.93 to 70.25 (average = 49.85), from 33.62 to 106.75 (average = 66.24) and from 1.91 to 30.13 (average = 6.67) respectively (as detailed in Table 2 and Fig. 4b). Samples from the Qianjiang Formation exhibit ICV values consistently exceeding 1, indicating limited clay mineral fractionation and immature sediment composition, thereby validating the efficacy of CIA in characterizing source rock weathering regimes (Cox et al., 1995). To compensate for the effects of K-metasomatism, corrections were implemented to the CIA in this study. The corrected CIA* values exhibit a range of 17.40 to 68.29, averaging 51.36 (Table 2). The minimal discrepancy between corrected and original values indicates negligible potassic metasomatism. The A-CN-K ternary diagram reveals that most sample points cluster within regions indicative of weak chemical weathering and cold, arid climatic conditions (Fig. 3a). The Molybdenum Enrichment Factor (Mo_{EF}) and Uranium Enrichment Factor (U_{EF}) values range from 3.52 to 47.63 (average = 14.40) and 1.95 to 6.04 (average = 2.89), respectively, as shown in Fig. 11b.

Trace element analysis reveals that only Sr and Mo exhibit significant enrichment, while Ba shows considerable variability. Other elements are generally depleted relative to the PAAS (Table 2). The Th/Sc and Zr/Sc ratios range from 0.98 to 1.38 and from 6.93 to 15.98, respectively (Fig. 4a). The Sr/Ba and B/Ga ratios vary from 0.32 to 7.99 (average = 2.63) and from 0.12 to 33.71 (average = 10.67) (Fig. 9a). Co (ppm) × Mn (wt%) and Cd/Mo are range from 0.18 to 1.18 (average = 0.72) and from 0.01 to 0.26 (average = 0.04) (Fig. 11a).

4.3. Maceral composition and vitrinite reflectance

The organic matter is predominantly composed of liptinite,

Table 2
Major and trace element parameters of samples from Eq^3 of Qianjiang Formation in Qianjiang Depression, Jianghan Basin, China.

Sample ID	Major element (wt%)								Major and trace element calculation parameters																	
	SiO_2	Al_2O_3	CaO	MgO	Na_2O	K_2O	P_2O_5	MnO	CIA	PIA	WIP	ICV	CIA*	Mo_{EF}	U_{EF}	P/Ti	K_2O/Al_2O_3	Ga/Rb	Al/Si	Th/Sc	Zr/Sc	Sr/Ba	B/Ga	Cd/Mo	Co (ppm) × Mn (wt%)
Q1–1	26.89	5.75	26.49	3.98	1.35	9.39	0.19	0.05	45.41	42.46	33.62	11.33	49.27	47.63	6.04	1.48	0.40	0.12	0.25	1.12	9.62	5.08	13.97	0.01	0.58
Q1–2	41.97	9.65	13.20	5.18	2.23	15.62	0.18	0.05	45.84	43.24	71.94	4.93	49.55	21.54	3.28	0.94	0.39	0.13	0.27	1.38	10.42	3.48	14.45	0.02	0.56
Q1–3	50.64	12.94	6.54	4.81	2.65	20.49	0.17	0.05	47.95	46.61	85.64	2.80	52.12	3.99	2.48	0.57	0.38	0.10	0.30	1.21	8.97	0.64	28.81	0.03	0.53
Q1–4	47.62	12.92	7.41	4.66	2.37	18.34	0.16	0.04	53.75	55.17	66.20	2.79	54.37	13.02	2.71	0.63	0.24	0.15	0.32	1.19	9.74	1.01	10.16	0.03	0.58
Q1–5	32.07	9.04	14.05	7.75	2.11	13.18	0.16	0.07	49.73	49.64	63.08	5.99	49.37	26.34	4.03	0.87	0.22	0.16	0.33	1.05	10.77	2.04	3.48	0.02	0.89
Q1–6	49.33	13.24	6.60	3.25	2.45	18.65	0.28	0.05	54.01	55.43	62.41	2.33	54.21	14.56	2.77	1.03	0.22	0.14	0.32	1.07	8.55	1.11	11.40	0.03	0.77
Q1–7	52.25	6.30	17.83	2.31	7.69	15.37	0.11	0.03	19.03	15.93	106.75	8.60	17.40	9.24	2.03	0.86	0.22	0.16	0.14	1.02	7.75	7.99	0.12	0.03	0.18
Q1–8	36.70	10.16	17.24	4.47	3.29	16.71	0.23	0.06	41.43	37.95	78.07	5.31	42.24	10.86	3.49	1.05	0.32	0.14	0.33	1.03	6.93	5.72	2.35	0.02	0.72
Q1–9	43.97	11.79	15.21	2.31	3.38	18.63	0.27	0.05	44.25	41.99	74.72	3.86	44.93	10.37	3.21	1.03	0.29	0.14	0.32	1.21	8.83	1.36	5.81	0.04	0.79
Q1–10	26.58	5.44	24.66	8.13	1.67	8.29	0.12	0.06	44.56	43.13	51.82	13.14	43.40	4.48	2.24	0.84	0.22	0.18	0.24	1.10	15.98	5.51	5.73	0.26	0.39
Q1–11	51.00	12.98	9.72	2.69	1.25	17.94	0.13	0.07	61.43	68.45	53.49	2.68	66.21	12.48	2.05	0.54	0.29	0.14	0.30	1.02	9.44	0.59	8.26	0.03	1.01
Q1–12	11.01	3.02	26.34	15.18	0.88	4.92	0.17	0.16	42.93	39.69	61.03	30.13	44.47	9.01	1.95	2.74	0.34	0.15	0.32	0.98	15.44	2.05	6.63	0.04	0.69
Q1–13	55.59	14.12	6.77	2.35	1.26	20.03	0.15	0.07	60.58	68.64	60.59	2.11	67.44	3.52	2.28	0.46	0.33	0.10	0.30	1.20	9.40	0.32	33.71	0.04	0.77
Q1–14	52.85	15.33	5.66	3.03	1.40	21.36	0.14	0.08	61.43	69.16	63.95	1.98	67.14	11.44	2.30	0.42	0.30	0.15	0.34	1.11	9.63	1.10	11.23	0.03	1.18
Q1–15	53.27	14.43	6.85	2.62	1.22	20.23	0.13	0.08	61.65	70.25	60.28	2.14	68.29	17.55	2.54	0.39	0.32	0.16	0.32	1.04	10.87	1.48	3.90	0.02	1.10

accounting for 0.44 % to 10.43 % of the total rock composition, with an average of 3.74 % (Table 3). Notably, liptinite in the Eq^3 strata of the Qianjiang Depression is almost exclusively alginite, while exinite is exceptionally rare. Under fluorescence microscopy, alginite displays a distinct bright yellow fluorescence (Liu et al., 2023a; Luo et al., 2018; Pakdel et al., 1999; Scott, 2002; Wu et al., 2022a; Fig. 5b, d, h and j). Two subtypes of alginite—lamalginite and telalginite—are identified. Lamalginite, the dominant subtype, forms dense, continuous thin layers that often span entire thin sections (Scott, 2002; Yu et al., 2024; Fig. 5b, h and j). In contrast, telalginite exhibits an elliptical morphology with well-defined margins (Hutton and Hower, 1999; Kus et al., 2017; Xie et al., 2014; Fig. 5d). Vitrinite and inertinite contents are relatively low, ranging from 0.06 % to 0.64 % (average = 0.31 %) and 0.03 % to 0.10 % (average = 0.06 %), respectively (Table 3). Vitrinite is further divided into two subgroups: collotelinite, which appears gray-black under reflected light and brown under fluorescence (Davis et al., 1990; Ottenjann, 1988; Xiao et al., 2002; Fig. 5g, h, and k), and telinite, characterized by an elliptical morphology with a cavity structure, appearing off-white under reflected light and black under fluorescence (Hackley and Martinez, 2007; Hower et al., 2008; Mukherjee et al., 2021; Pickel et al., 2017; Fig. 5e, f and g). Pyrite is ubiquitously distributed throughout the samples, frequently forming aggregates and occasionally occurring as inclusions within the organic matter (Song et al., 2021; Fig. 5a, c, i, and k). Additionally, R_o values range from 0.42 to 0.56 (average = 0.47), consistent with the low thermal maturity of the samples (Table 3).

4.4. Biomarker parameters

4.4.1. Saturated hydrocarbon

Biomarker parameters for saturated hydrocarbons are summarized in Table 4, with *m/z* 125, *m/z* 191 and *m/z* 217 fragmentograms, along with total ion chromatograms (TIC) of two representative samples, illustrated in Fig. 6. Pristane (Pr) and phytane (pH) are identified from TIC, whereas terpanes and steranes are obtained from *m/z* 191 and *m/z* 217 respectively. Carbon Preference Index (CPI) values range from 0.76 to 1.06 (average = 0.92), suggesting a trend toward even-carbon predominance approaching equilibrium with increasing depth (Fig. 6a and b). Long-chain *n*-alkanes ($\geq$ *n*-C_{22}) dominate the detectable *n*-alkane distribution (the carbon number from *n*-C_{16} to *n*-C_{40}), as indicated by low *n*-C_{21-}/*n*-C_{22+} ratios (0.15–0.70, average = 0.34) and high terrigenous/aquatic ratios (TAR) (0.80–7.16, average = 2.80). TIC profiles further reveal a progressive increase in the abundance of short-chain *n*-alkanes with depth (Fig. 6a and b). The Pr/*n*-C_{17} and Ph/*n*-C_{18} ratios range from 0.97 to 2.58 (average = 1.58) and from 1.95 to 7.31 (average = 4.33), respectively (Fig. 7a). Moreover, the samples exhibit notably low Pr/Ph ratios, ranging from 0.11 to 0.40, with a mean value of 0.26 (Table 4).

Tricyclic and tetracyclic terpenes are also present in the samples (Table 4; Fig. 6c and d). The ratios of C_{19} tricyclic terpenes (C_{19}TT) and C_{24} tetracyclic terpenes (C_{24}TeT) relative to C_{23} tricyclic terpenes (C_{23}TT) range from 0.03 to 0.53 (average = 0.15) and from 0.69 to 0.96 (average = 0.82), respectively. Extended tricyclic terpanes ratio (ETR), calculated as shown in Table 4, ranges from 0.52 to 10.32 (average = 3.36) (Holba et al., 2001). Ts/(Ts + Tm) ratios exhibit a decreasing trend with depth, varying from 0.04 to 0.61 (average = 0.39). Hopane distributions display notable features (Fig. 6c and d), with gammacerane (Gamm) and β-carotane being particularly abundant (Fig. 6a–d). The Gamm/C_{30} ($\beta\alpha + \alpha\beta$) hopane ratios ranging from 0.42 to 1.60 (average = 1.11) and from 0.02 to 0.30 (average = 0.11), respectively (Fig. 7d).

A ternary diagram of C_{27}-C_{28}-C_{29} regular steranes reveals distinct compositional trends, as depicted in Fig. 7c. Relative percentages of C_{27}, C_{28}, and C_{29} regular steranes are distributed as follows: C_{27} ranges from 22.30 % to 57.41 % (average = 36.64 %), C_{28} from 16.39 % to 31.13 % (average = 23.02 %), and C_{29} from 26.20 % to 48.36 % (average = 40.35 %). C_{27}/C_{29} and C_{28}/C_{29} radios exhibit significant variability,

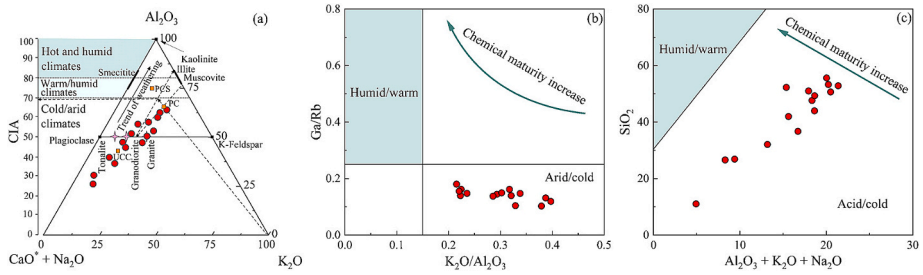

Fig. 3. (a) A-CN-K ternary diagram of the studied sample (Fedo et al., 1995). UCC = upper continental crust; PC = pre-metasomatized composition; PCS = paleoproterozoic cratonic shale. (b) K_2O/Al_2O_3 versus Ga/Rb (Qiao et al., 2022). (c) $Al_2O_3 + K_2O + Na_2O$ versus SiO_2 (Suttner and Dutta, 1986).

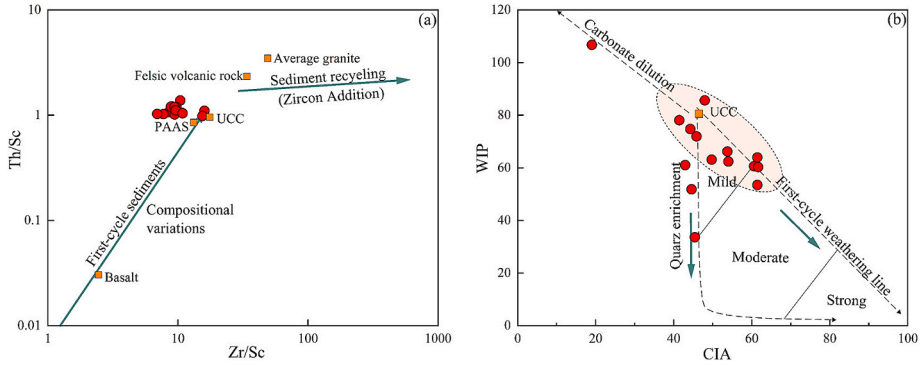

Fig. 4. Diagrams of (a) Zr/Sc versus Th/Sc (McLennan, 1993), (b) CIA versus WIP (Garzanti et al., 2013). Valid data within the circle explaining the sediment recycling of organic-rich shales.

Table 3
Quantitative data of maceral components from studied rock slices of Qianjiang Formation in Qianjiang Depression, Jianghan Basin, China.

Sample ID	Vitrinite (%)	Inertinite (%)	Liptinite (%)	Mineral (%)	L/(V + I)	R_o (%)
Q1–1	0.64	0.10	10.43	88.83	10.45	0.42
Q1–2	0.63	0.07	5.53	93.77	7.95	0.43
Q1–3	0.52	0.10	1.07	98.30	1.72	0.44
Q1–4	0.31	0.06	9.38	90.25	10.31	0.44
Q1–5	0.26	0.03	8.63	91.08	11.95	0.45
Q1–6	0.20	0.03	7.13	92.64	21.70	0.45
Q1–7	0.16	0.03	2.00	97.81	6.78	0.46
Q1–8	0.30	0.07	5.41	94.23	10.93	0.47
Q1–9	0.06	0.03	1.13	98.78	11.67	0.47
Q1–10	0.39	0.07	0.92	98.62	2.00	0.45
Q1–11	0.39	0.07	1.34	98.20	1.81	0.47
Q1–12	0.07	0.07	0.71	99.15	5.25	0.49
Q1–13	0.17	0.03	1.25	98.55	6.17	0.55
Q1–14	0.20	0.07	0.44	99.29	1.63	0.54
Q1–15	0.27	0.03	0.74	98.96	2.44	0.56

L/(V + I), liptinite/(vitrinite + inertinite).

spanning 0.48 to 2.19 (average = 1.00) and 0.18 to 1.21 (average = 0.63), respectively (Table 4). C_{27}-C_{28}-C_{29} regular steranes display a characteristic "L"-type distribution, as illustrated in Fig. 6e and f.

4.4.2. Aromatic hydrocarbon

The analyzed samples exhibit a predominance of low-molecular-weight polycyclic aromatic hydrocarbons (PAHs), particularly 2- and 3-ring structures. Fig. 12 presents characteristic mass chromatograms quantifying key molecular markers: phenanthrene (P, *m/z* 178), methylphenanthrenes (MPs, *m/z* 192) including 1-, 2-, 3-, and 9-methyl isomers, dimethylphenanthrenes (DMPs, *m/z* 206), trimethylnaphthalenes (TMNs, *m/z* 170), fluorene (F, *m/z* 166), dibenzofuran (DBF, *m/z* 168), dibenzothiophene (DBT, *m/z* 184), retene (Ret, *m/z* 234), and triaromatic steroids (TAS; *m/z* 231). Three diagnostic geochemical indices, the Methylphenanthrene Index (MPI-1) and two methylphenanthrene ratios (F_1 and F_2), are employed to assess thermal maturity (Chen et al., 2010; Kvalheim et al., 1987). All samples demonstrate consistently low thermal alteration parameters: MPI-1 = 0.61–0.96 (mean 0.76), F_1 = 0.37–0.50 (mean 0.41), and F_2 = 0.22–0.34 (mean 0.26) (Table 5). The dibenzothiophene/phenanthrene (DBT/P) ratio further corroborates this trend, yielding exceptionally low values of 0.02–0.87 (mean 0.21) (Fig. 7b). Relative proportions of fluorene (F), dibenzofuran (DBF), and dibenzothiophene (DBT) are also analyzed. Results indicate fluorene constitutes 0.19–18.84 % (average = 5.13 %), dibenzofuran accounts for 0.11–9.15 % (average = 1.99 %), and dibenzothiophene dominates at 72.00–99.70 % (average = 92.88 %) of the total composition (Fig. 9b). Log plots of partial aromatic biomarker ratios are shown as Fig. 13a–c.

5. Discussion

5.1. Thermal maturity of organic matter

The studied samples exhibit consistently low R_o values, which unequivocally indicate that the organic matter is in a immature to low-maturity stages (Table 3). This interpretation is further corroborated by pyrolysis-derived T_{max} values, which are consistently below the widely accepted threshold of 445 °C, a critical benchmark for identifying low thermal maturity in organic-rich sediments (Peters and Cassa, 1994). Moreover, Luo et al. (2018) demonstrated that the depletion of polar components, such as asphaltenes and non-hydrocarbons, provides additional evidence for low maturity conditions. The samples collected from the Tankou area exhibit geochemical and petrographic characteristics that are remarkably analogous to those of low mature shales from the Lucaogou Formation in the Junggar Basin (Qiao et al., 2023). Specifically, these similarities are manifested in the pronounced fluorescence intensity and elevated concentrations of alginite, both of which are diagnostic features of immature organic matter (Fig. 5).

In continental shales characterized by low thermal maturity, n-alkanes typically display a pronounced odd-carbon predominance, a

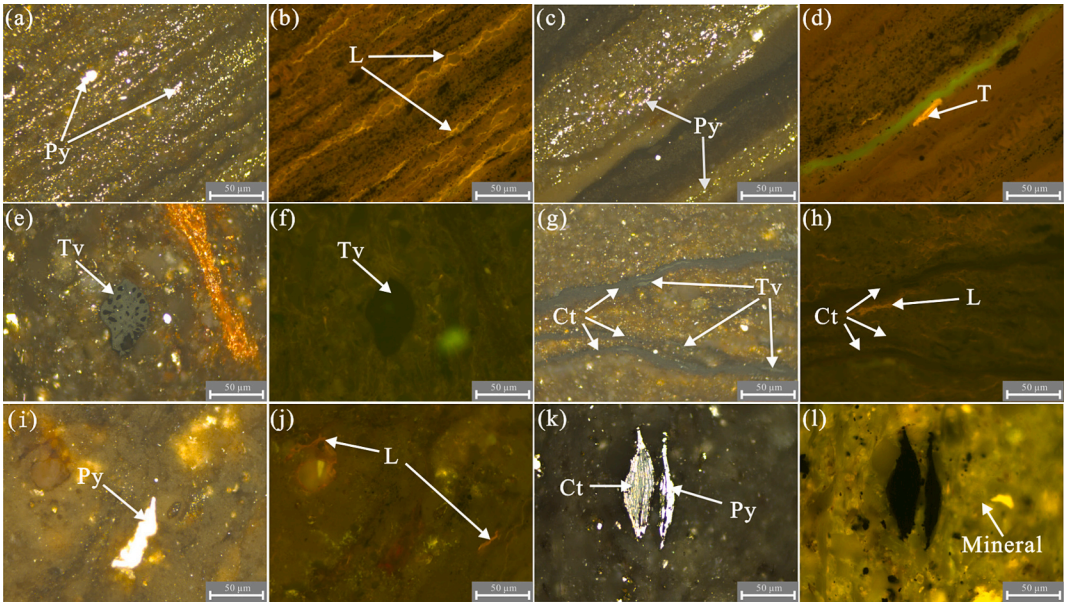

Fig. 5. Photomicrographs showing Ct, Tv, L, T, Py and minerals in Eq^3 from Qianjiang Depression. The images presented are captured in patterns of reflective white light mode (a, c, e, g, i, k) and fluorescent light mode (b, d, f, h, j, l). The photo contains collotelinite (Ct in g, h, and k), telinite (Tv in e, f and g), lamalginite (L in b, h and j), telalginite (T in d) and pyrite (Py in a, c, i and k).

Table 4
Saturated hydrocarbon biomarker parameters of Eq^3, the thrid member Qianjiang Formation in Qianjiang Depression, Jianghan Basin, China.

Sample ID	*N*-alkanes and isoprene						Terpane					Sterane	
	n-C_{21-}/n-C_{22+}	TAR	CPI	Pr/n-C_{17}	Ph/n-C_{18}	Pr/Ph	$C_{19}TT/(C_{19}TT + C_{23}TT)$	$C_{24}TeT/(C_{24}TeT + C_{23}TT)$	Ts/(Ts + Tm)	ETR	Gamm/C_{30} (βα + αβ)	C_{27}/C_{29}	C_{28}/C_{29}
Q1–1	0.29	3.59	0.91	1.14	2.71	0.27	0.12	0.77	0.55	2.82	1.15	0.58	0.72
Q1–2	0.29	2.66	0.91	0.97	1.95	0.30	0.18	0.69	0.57	1.49	1.00	0.48	0.70
Q1–3	0.15	6.43	0.91	1.95	3.88	0.20	0.09	0.84	0.47	2.59	1.27	0.57	0.56
Q1–4	0.15	7.16	0.92	2.02	3.85	0.15	0.07	0.85	0.49	2.61	1.28	0.53	0.43
Q1–5	0.38	1.62	0.76	2.58	3.30	0.40	0.53	0.77	0.61	0.52	0.87	0.69	0.83
Q1–6	0.28	3.63	0.89	1.20	2.66	0.28	0.14	0.71	0.61	1.73	0.82	0.62	0.38
Q1–7	0.24	3.27	0.86	1.78	3.73	0.25	0.09	0.80	0.58	3.31	1.60	0.79	0.89
Q1–8	0.36	2.22	0.87	1.25	2.70	0.35	0.12	0.69	0.57	2.51	0.84	0.73	1.21
Q1–9	0.34	1.71	0.82	1.83	4.49	0.30	0.26	0.87	0.21	1.85	1.60	0.71	0.49
Q1–10	0.35	1.77	0.76	2.15	4.84	0.26	0.34	0.86	0.24	1.21	1.24	1.21	0.75
Q1–11	0.70	0.80	1.06	1.03	6.41	0.19	0.03	0.96	0.04	10.32	1.37	2.19	0.68
Q1–12	0.42	1.53	1.00	1.34	4.15	0.28	0.11	0.77	0.17	3.17	0.42	0.97	0.38
Q1–13	0.58	0.95	1.00	1.27	5.97	0.22	0.08	0.81	0.15	6.01	0.48	1.40	0.82
Q1–14	0.28	2.80	1.04	1.35	7.31	0.11	0.05	0.94	0.05	7.84	1.38	1.94	0.45
Q1–15	0.35	1.82	1.02	1.80	6.94	0.30	0.06	0.90	0.50	2.35	1.30	1.63	0.18

TAR, Terrigenous/aquatic ratio, (n-C_{27} + n-C_{29} + n-C_{31})/(n-C_{15} + n-C_{17} + n-C_{19}); CPI, carbon preference index, 2[n-C_{23} + n-C_{25} + n-C_{27} + n-C_{29}]/[n-C_{22} + 2{n-C_{24} + n-C_{26} + n-C_{28}} + n-C_{30}]; Pr, pristane; Ph, phytane; TT, tricyclic terpanes; TeT, tetracyclic terpane; Ts, C_{27} 17α(H)-22,29,30-trisnorneohopane; Tm, C_{27} 18α(H)-22,29,30-trisnorhopane; ETR, (C_{28} TT + C_{29} TT)/Ts ratio; Gamm/C_{30} (βα + αβ), Gamm/ C_{30} (βα + αβ) hopane; C_{27}/C_{29}, C_{27} sterane/C_{29} sterane; C_{28}/C_{29}, C_{28} sterane/C_{29} sterane; C_{29} 20S/(20S + 20R).

feature that gradually diminishes as organic matter undergoes thermal maturation (Wehner et al., 1986). Intriguingly, the TIC of shallow-depth samples in this study reveals a relatively distinct even-numbered carbon advantage, with the predominant peaks corresponding to n-C_{24}, n-C_{26}, and n-C_{28} (Fig. 6a). Furthermore, CPI values for these samples are consistently below 1.00 (Table 4). Such even-carbon predominance has been previously documented in specific carbonate rocks and hypersaline environments (Moldowan et al., 1985; Peters et al., 2005). This accelerated isomerization can lead to premature equilibrium of hopane configurations, even in otherwise immature samples. The maturity parameter Ts/(Ts + Tm) exhibits a distribution pattern that is likely influenced by lithological factors and the oxidative conditions of the sedimentary environment (Kolaczkowska, 1990; Seifert and Moldowan, 1978; Table 4). Given its sensitivity to clay minerals, low Ts/(Ts + Tm) ratios in deep samples often indicates high carbonate mineral content (Fan et al., 1987; Rullkötter and Marzi, 1988; Rullkötter et al., 1985). The observation is corroborated by C_{27}-C_{28}-C_{29} regular steranes distributions. Shallow-depth samples are characterized by $C_{29} > C_{27} > C_{28}$, indicating higher clay content, while deeper samples exhibit $C_{27} > C_{29} > C_{28}$. aligning with increased C_{27}/C_{29} ratios at greater depths as illustrated in Fig. 6e and f.

Aromatic hydrocarbon biomarkers are widely recognized for their stability during diagenetic evolution, therefore, they are frequently used to assess the maturity of organic matter (Luo et al., 2018; Peters et al., 2005; Synnott et al., 2023; van Aarssen et al., 2000). In this study, the MPI-1 indicates low to moderate maturity level (Ji et al., 2014; Sachsenhofer et al., 2006; Szczerba and Rospondek, 2010; Table 5). Additionally, methylphenylene ratios F_1 and F_2 both fall within the low-to-medium range, consistent with the proof of R_o and T_{max} values (Chen et al., 2010; Fig. 8a). TAS cracking ratio, related to the thermal evolution

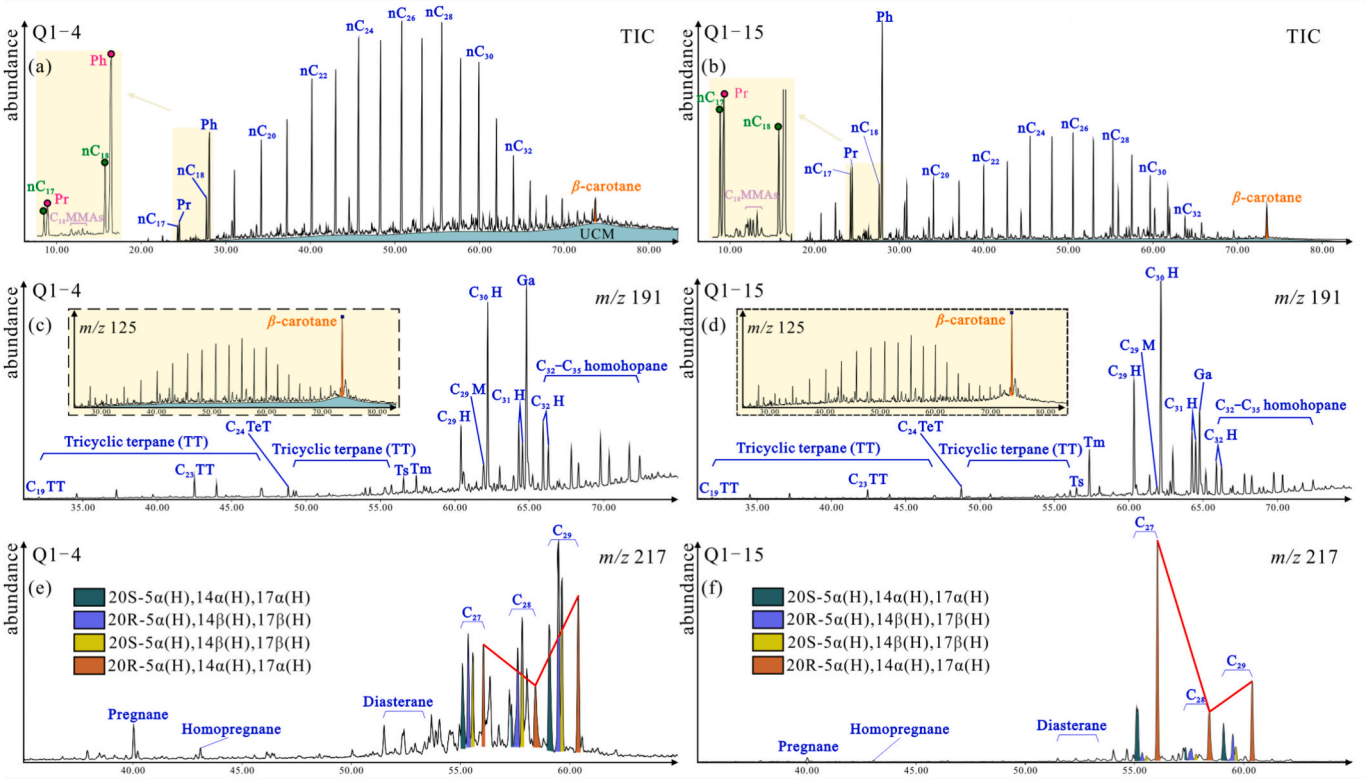

Fig. 6. TIC and mass chromatograms of two samples from Eq[3] in Tankou area. (a), (c) and (e) are from QYP1–1929.2 m, while (b), (d) and (f) are from QYP1–2661.0 m. (a) and (b) come from TIC of the two samlpes, showing the distribution of *n*-alkanes, isoprenoids and *β*-carotane. (c) and (d) are derived from the $m/z = 191$ and $m/z = 125$ fragmentograms of the two samples, showing the partial distribution of tricyclic terpenes, tetracyclic terpenes and hopanes, *β*-carotane, as well as their derivatives. (e) and (f) are derived from the $m/z = 217$ fragmentograms of the two samples, showing the partial distribution of regular steranes and diasteranes.

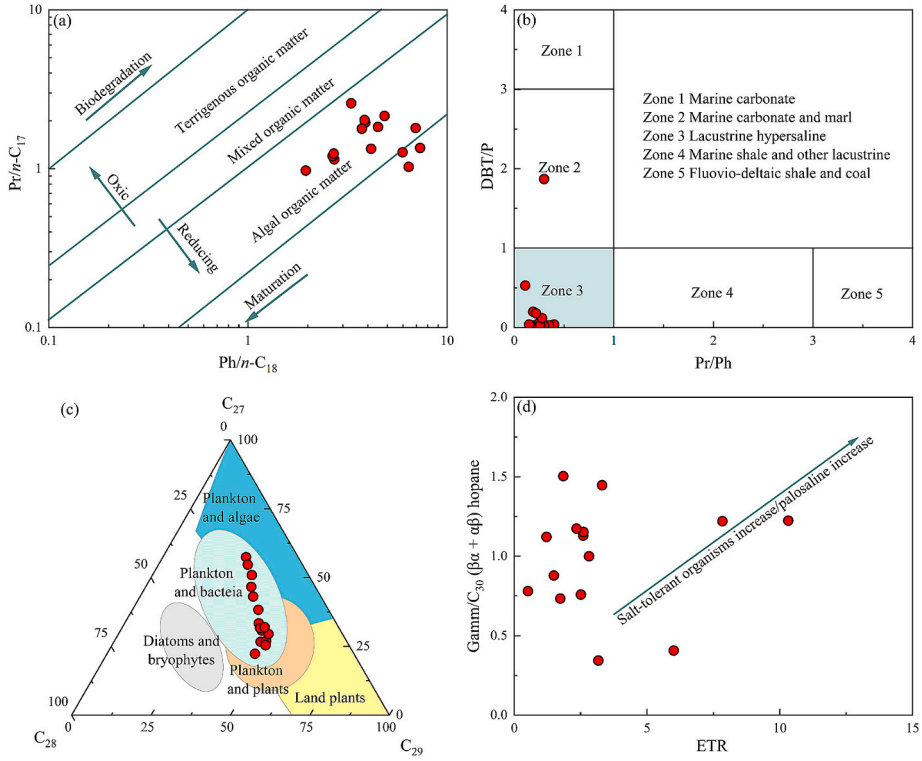

Fig. 7. (a) Ph/*n*-C_{17} versus Pr/*n*-C_{18}, indicating that the main source of organic matter is algae; (b) Pr/Ph versus DBT/P, proved that the studid area is a high salinity lacustrine sedimentary environment; (c) ternary plot of C_{27}–C_{28}–C_{29} regular sterane relative content; (d) Gamm/C_{30} (βα + αβ) hopane versus ETR, showing that the study area is mainly composed of saline deposits and salt-tolerant organisms.

Table 5
Aromatic hydrocarbon biomarker parameters of Eq[3], the thrid member Qianjiang Formation in Qianjiang Depression, Jianghan Basin, China.

Sample ID	Aromatic hydrocarbon											
	MPI-1	F_1	F_2	DBT/P	Log (1,2,7-TMN/1,3,7-TMN)	Log (1,2,5-TMN/1,3,6-TMN)	Log (1,2,5-TMN/1,3,6-TMN)	Log (1-MP/9-MP)	Log [1,7-DMP/(1,3 − +3,9 − + 2,10 − +3,10-DMP)]	Log (Retene/9-MP)	$(C_{20} + C_{21})/(C_{20} + C_{21} + C_{26} + C_{27} + C_{28})$	$C_{20}/(C_{20} + C_{28}$ (20R))
Q1–1	0.61	0.39	0.23	0.02	0.71	0.38	0.38	−0.08	−0.36	−1.38	0.14	0.31
Q1–2	0.62	0.40	0.23	0.02	0.64	0.42	0.42	−0.08	−0.35	−0.97	0.20	0.44
Q1–3	0.68	0.37	0.22	0.03	0.13	−0.05	−0.05	−0.04	−0.33	−0.99	0.09	0.21
Q1–4	0.78	0.37	0.24	0.04	−0.09	−0.46	−0.46	−0.02	−0.26	0.38	0.09	0.21
Q1–5	0.72	0.40	0.25	0.04	0.64	0.57	0.57	−0.04	−0.28	−0.81	0.19	0.42
Q1–6	0.75	0.38	0.23	0.03	−0.10	−0.44	−0.44	−0.04	−0.30	−0.84	0.15	0.33
Q1–7	0.73	0.37	0.23	0.06	0.27	−0.02	−0.02	−0.02	−0.29	−1.20	0.16	0.31
Q1–8	0.65	0.39	0.24	0.03	0.66	0.50	0.50	−0.03	−0.27	−0.91	0.14	0.34
Q1–9	0.74	0.41	0.28	0.02	0.43	0.33	0.33	−0.01	−0.23	−0.74	0.13	0.28
Q1–10	0.84	0.39	0.27	0.03	0.01	−0.46	−0.46	−0.04	−0.25	−0.99	0.07	0.19
Q1–11	0.96	0.49	0.32	0.20	0.07	0.09	0.09	−0.14	−0.25	−0.54	0.03	0.08
Q1–12	0.83	0.43	0.26	0.12	0.14	−0.22	−0.22	−0.11	−0.27	−0.76	0.04	0.10
Q1–13	0.87	0.46	0.28	0.18	−0.03	−0.21	−0.21	−0.10	−0.14	−0.57	0.03	0.09
Q1–14	0.86	0.43	0.29	0.53	0.92	0.61	0.61	−0.11	−0.27	−0.29	0.03	0.08
Q1–15	0.81	0.50	0.34	1.87	0.92	0.61	0.61	−0.10	−0.21	−0.61	0.03	0.12

TMN, trimethylnaphthalene; MP, methylphenanthrene; DMP, dimethylphenanthrene; MPI-1, methylphenanthrene index; F_1 and F_2, methylphenanthrene ratio; DBT/P, dibenzothiophene/phenanthre.

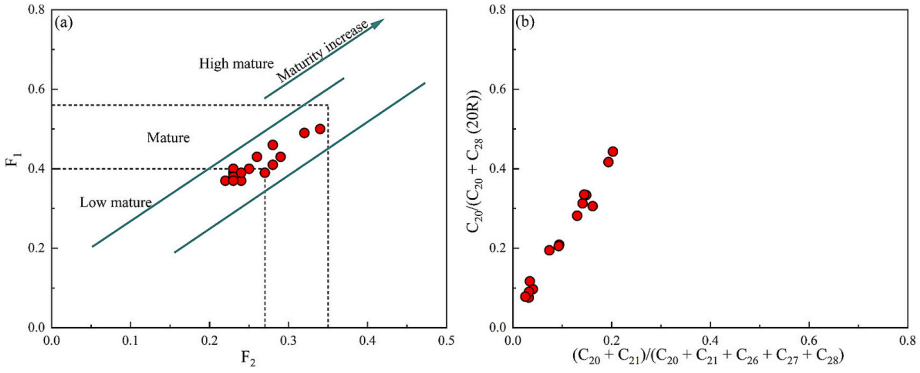

Fig. 8. Diagrams of (a) methylphenanthrene ratio F_2 versus F_1, indicating the results of low mature to mature (Chen et al., 2010), and (b) $(C_{20} + C_{21})/(C_{20} + C_{21} + C_{26} + C_{27} + C_{28})$ versus $C_{20}/(C_{20} + C_{28}$ (20R)) triaromatic steroids.

of organic matter, is widely used as a maturity index (Thompson-Butler et al., 2019). $(C_{20} + C_{21})/(C_{20} + C_{21} + C_{26} + C_{27} + C_{28})$ versus $C_{20}/(C_{20} + C_{28}$ (20R)) triaromatic steroids provides good indication of low ripeness to medium maturity (Fig. 8b). Although aromatic hydrocarbons exhibit greater thermal stability compared to saturated hydrocarbons, their geochemical parameters demonstrate systematic discrepancies with R_o in reconstructing thermal maturity. This divergence may stem from the selective catalytic influence of saline minerals on organic matter, preferentially accelerating the transformation of hydrogen-rich components (e.g., lamalginite) during early diagenesis (Johns and Shimoyama, 1972; Horsfield and Douglas, 1980). In summary, R_o, pyrolysis T_{max}, saturated and aromatic hydrocarbon parameters collectively indicate that the samples from the Qianjiang Depression exhibit immature to low-mature level.

5.2. Provenance of source rock

Terrigenous clastic material supply is an essential prerequisite for forming clastic source rocks. Provenance of clastic sediments controls sedimentary facies and lithological assemblages, and significantly influences organic matter enrichment and hydrocarbon generation potential (Qiao et al., 2023; Salah et al., 2023). In lacustrine sediments, SiO_2 and Al_2O_3 typically signify terrigenous inputs, whereas CaO and MgO are primarily derived from carbonate minerals. Compared to PAAS, the analyzed samples exhibit a lower proportion of terrigenous material and a higher contribution from chemical deposition. The elevated Na_2O concentrations further underscores the prevalence of a strong evaporative environment (Taylor and McLennan, 1985; Table 2). These findings align with observations from other research areas within the Qianjiang Formation of the Qianjiang Depression in the Jianghan Basin (Ge et al., 2023; Kong et al., 2022). The Si and Al serve as geochemical proxies for distinguishing between coarse-grained detritus (e.g., quartz, plagioclase and K-feldspar) and fine-grained detritus (e.g., clay mineral assemblages), respectively. Consequently, the molar Al/Si ratio has been widely adopted in sedimentary geology as a robust quantitative indicator for assessing the intensity of hydraulic sorting processes during clastic sediment transport and deposition (Bouchez et al., 2011; Lupker et al., 2012). The mol Al/Si ratio in the sample is poorly correlated with WIP (Fig. 14a) and CIA (Fig. 14b), indicating that they are not affected by hydraulic sorting. Zirconium (Zr), predominantly sourced from zircon minerals, remains stable during sedimentary processes, while scandium (Sc) and thorium (Th) are enriched in mafic and felsic rocks, respectively (Mclennan et al., 1990; Qiao et al., 2023; Fig. 4a). The Zr/Sc versus Th/Sc ratio is a widely utilized index for assessing compositional maturity and sedimentary recycling. Proximity to the first-cycle line suggests that the rocks have undergone minimal weathering and retain their original composition (McLennan, 1993; Taylor and McLennan, 1985). The sample plot locations within the study area exhibit

similarities to PAAS and upper continental crust (UCC), indicating that they are products of the first sedimentary cycle (Fig. 4a). In addition, the absence of quartz enrichment in most samples indicates that the stable mineral did not experience significant accumulation. Since WIP values fluctuate significantly, the CIA derived from the other part of the sample also indicates no multiple recycling process (Fig. 4b). It is imperative to note that samples exhibiting deviations of CIA and WIP indices beyond the valid range necessitate careful consideration when interpreting paleoclimatic conditions and organic matter enrichment drivers. These findings imply that the organic matter in the source rocks and the associated sediments are of in-situ origin, thereby representing the primary depositional environment.

The hydrocarbon generation potential of source rocks is fundamentally governed by the input of organic matter. Pr and Ph are primarily derived from the phytol side chain of chlorophyll *a* in photosynthetic organisms (Brooks et al., 1969; Peters et al., 2005; Powell and Mckirdy, 1973). The Pr/*n*-C_{17} versus Ph/*n*-C_{18} cross-plot reveals that the organic matter is predominantly sourced from aquatic organisms, particularly algae (Fig. 7a). Exceptionally high phytane concentrations may also be attributed to algal blooms (Ge et al., 2023; Fig. 6a and b). The *n*-alkanes are dominated by long-chain *n*-alkanes ($> C_{21}$), displaying a rear-peak distribution pattern with distinct even-carbon predominance (Fig. 6a). With depth increasing, the proportion of short-chain *n*-alkanes rises, transitioning the distribution to a bimodal pattern and eliminating the even-carbon preference (Fig. 6b). Rear-peak *n*-alkane distributions are conventionally interpreted as indicative of higher plant-derived organic matter, typically accompanied by pronounced odd-carbon predominance (Grimalt and Albaiges, 1987). However, all source rock samples from the Qianjiang Formation exhibit dominant peak carbons exclusively at even-numbered positions (C_{16}, C_{24}, C_{26} and C_{28}), simultaneously demonstrating both even-carbon predominance and rear-peak characteristics. Decades of research have revealed that long-chain, even-carbon-predominant distributions in sedimentary rocks or crude oils frequently originate from hypersaline, strongly reducing environments, potentially linked to microbial contributions from bacteria or salt-tolerant algae (Jeng and Huh, 2008; Sinninghe Damsté et al., 1995; Qiao et al., 2021). Compared to long-chain *n*-alkanes, short-chain *n*-alkanes exhibit depletion, as evidenced by relatively low *n*-C_{21-}/*n*-C_{22+} ratios, which indicate a limited terrestrial input (Table 4). C_{19} tricyclic terpenes, primarily derived from diterpenoid compounds produced by vascular plants, signify input from higher plants. In contrast, other tricyclic terpenes and C_{24} tetracyclic terpenes are closely associated with algal sources (Peters et al., 2005; Sinninghe Damsté et al., 1995). Despite some terrestrial input, the very low $C_{19}TT/(C_{19}TT + C_{23}TT)$ ratios and exceedingly high $C_{24}TeT/(C_{24}TeT + C_{23}TT)$ ratios underscore the dominance of algal-derived organic matter (Table 4). Additionally, the elevated C_{24} tetracyclic terpene content is linked to the presence of carbonate rocks and evaporites (Connan et al., 1986; Peters et al., 2005). Sterane distributions further elucidate the sources of organic matter. C_{27} steranes are typically derived from algae, C_{28} steranes from phytoplankton, and C_{29} steranes from terrigenous higher plants (Liu et al., 2023b; Peters et al., 2005; Waples and Machihara, 1991). The C_{27}-C_{28}-C_{29} ternary diagram indicates the organic matter is predominantly algae in origin, with minor contributions from higher plants and bacteria (Fig. 7c). The prominent peaks of gammacerane and β-carotene further suggest that the bacterial input is primarily from salt-tolerant bacteria (Fig. 6c and d).

1,2,7-TMN serves as a biomarker for angiosperm-derived organic matter, whereas 1,2,5-TMN predominantly originates from higher plants (Armstroff et al., 2006; Püttmann and Villar, 1987). The exceptionally low TMNs concentrations detected in Eq^3 from the Qianjiang Depression imply negligible terrestrial contributions (Fig. 12). Ratios of log (1,2,7-TMN/1,3,7-TMN) and log (1,2,5-TMN/1,3,6-TMN) preliminarily identify angiosperms as the primary source in a small amount of terrigenous parent material (Fig. 13a). Budzinski et al. (1995) established that isomer distributions of MPs, DMPs and TMPs effectively discriminate terrigenous and/or marine origins in source rocks. Specifically, elevated 1-MP and 9-MP abundances correlate with terrestrial and marine inputs, respectively. Retene and 1,7-DMP further associate with higher plant sources (van Aarssen et al., 2000; Qiao et al., 2024). Cross-plots of log (1,2,5-TMN/1,3,6-TMN) vs. log (1-MP/9-MP) and log [1,7-DMP/(1,3-+3,9-+2,10-+3,10-DMP)] versus log (Retene/9-MP) consistently demonstrate limited higher plant contributions to the source rock (Fig. 13b and c), which is consistent with the evidences of sterane and terpane compounds.

During the deposition of the Eq^3 interval, organic matter was predominantly derived from lower aquatic organisms, including bacteria and algae. Organic petrological analysis reveals that algae constitute over 90 % of the organic content, with minimal contributions from vitrinite and inertinite (Table 3). Very high L/(V + I) ratios can also demonstrate an important contribution from algae, consistent with biomarker evidence (Table 3). Lamalginites are more densely distributed than telalginites, suggesting the preservation of extensive layered algal mats (Liu et al., 2022). Additionally, the presence of telalginites indicates the development of colonial organisms (Pichevin et al., 2004; Fig. 5d). Hydrogen-rich higher plant tissues, such as sporinite and cutinite, are rarely observed. Telinite, characterized by distinct biological structures, is formed through the gelation of plant cell walls, indicating a terrigenous higher plant origin (Fig. 5e, f and g). Collotelinite may originate from the incorporation of superfine lipid substances during the gelation of plant materials (Guo, 1993). Furthermore, the pronounced abundance of submicroscopic components observed in high-TOC samples is indicative of microbial inputs (e.g., bacteria), thereby contributing to the organic enrichment of high-TOC source rocks as critical precursor materials (Ghassal et al., 2016; Fig. 15). The widespread occurrence of pyrite in shale samples and the reciprocal encapsulation of organic matter and pyrite further indicate vigorous sulfate-reducing bacterial activity during sedimentation, providing indirect evidence for the genesis of bituminite (Fig. 5). In breif, algae constitute the primary source of organic matter, with a minor contribution from higher terrestrial plants.

5.3. Paleoenvironment reconstruction

Paleoclimate is a fundamental driver controlling the intensity of weathering processes, the supply of terrigenous detrital materials, and the characteristics of aqueous environments (e.g., paleosalinity and redox conditions). Its influence extends across geological and environmental processes, shaping the composition and distribution of sediments, as well as the preservation of organic matter in depositional settings (Fan et al., 2020; Qiao et al., 2022). Chemical weathering, in particular, plays a significant role in altering the chemical composition of detrital sediments, primarily through the hydraulic sorting of minerals and elements (McLennan, 1993; Xu and Shao, 2018). Fedo et al. (1995) established a framework correlating the CIA with the intensity of chemical weathering. According to their classification, CIA values below 70 indicate weak chemical weathering under cold or arid climatic conditions, values between 70 and 80 suggest moderate chemical weathering in warm and humid climates, and values above 80 reflect intense chemical weathering in warm and humid environments. To account for potassium (K) metasomatism during diagenesis, the A-CN-K ternary diagram and the PIA are employed to validate these findings (Fig. 3a). The Eq^3 shales from the Tankou area exhibit low CIA and PIA values, indicative of a cold and arid climate with minimal chemical weathering (Table 2). Notably, unusually high concentrations of Na_2O in some samples resulted in significant reductions in the CIA and PIA calculations (Table 2; Fig. 3a). As a highly migratory major element, this enrichment reflects the preservation of large quantities of rock salt in a high salinity environment and no significant chemical weathering. The elevated levels of CaO, MgO, and Na_2O in these samples further underscore the dominant influence of chemical deposition. These characteristics may introduce considerable deviations when using chemical

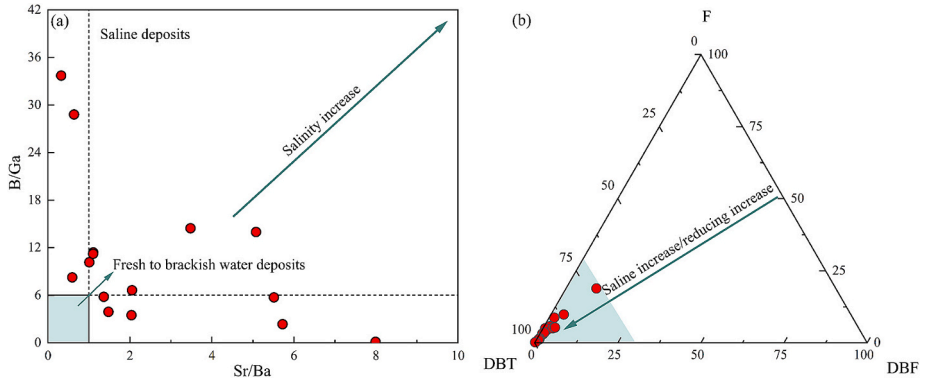

Fig. 9. (a) Sr/Ba versus B/Ga, indicating a highly reductive and ultra-high salinity environment, and the same consequence as (b) ternary diagram showing the relative concentration of DBF, F and DBT.

weathering indices such as CIA and PIA to infer paleoclimatic conditions (Xu and Shao, 2018). The granular clastic composition derived from the weathering of crystalline parent rocks in arid or humid climates exhibits distinct signatures (Suttner and Dutta, 1986). Suttner et al. (1981) demonstrated that the ratio of unstable clastic minerals (e.g., feldspar and lithic fragments) to polycrystalline quartz/total quartz serves as a reliable indicator of climatic conditions in sandstones. The geochemical application of SiO_2 versus $Al_2O_3 + K_2O + Na_2O$ bivariate plots has proven effective in characterizing the climatic conditions of clastic rocks (Qiao et al., 2023; Suttner and Dutta, 1986). The samples in this study, representing dolomitic shales of shallow lacustrine origin at medium to shallow depths, have not undergone long-distance transport or significant particle dissolution, thus meeting the criteria for bivariate plot analysis (Suttner et al., 1981; Suttner and Dutta, 1986). Despite considerable variability in SiO_2 content, the samples collectively reflect cold and acidic climatic conditions (Fig. 3c). This climatic interpretation is further supported by the binary plot of Gb/Rb versus K_2O/Al_2O_3 (Fig. 3b). It is noteworthy that some samples in Fig. 4b exhibit CIA and WIP values deviating from the effective domain. These significant deviations primarily result from dilution effects by carbonate minerals, rendering these outliers unsuitable for accurate paleoclimatic reconstructions. Nevertheless, within the comprehensive discriminant diagram employed for paleoclimate interpretation, all analyzed samples (including both deviated and valid datasets) consistently demonstrate coherent climatic implications pointing to cold and arid conditions. This consistency suggests that the impact of chemically precipitated minerals on paleoclimatic proxies remains statistically insignificant.

The redox state of sedimentary water is a pivotal factor controlling the preservation of organic matter (Burdige, 2007). Elemental geochemical parameters and biomarker indices are widely used to assess redox conditions, and their combined analysis provides a more accurate evaluation of organic matter preservation. The relationship among Pr, *n*-C_{17}, Ph and *n*-C_{18} is frequently employed to infer depositional environments (Peters et al., 2005). The Pr/*n*-C_{17} and Ph/*n*-C_{18} ratios in this study indicate that organic matter was preserved under reducing conditions (Fig. 7a). Exceptionally low Pr/Ph values further corroborate a strongly reducing paleoenvironment. Aromatic hydrocarbon biomarkers, such as DBT, F and DBF are thought to originate from the same biological precursors due to their similar chemical structures (Luo et al., 2018; Zhang and Philp, 2010). Elevated DBT concentrations relative to DBF are indicative of reducing conditions, whereas the opposite trend suggests an oxidizing environment (Hughes et al., 1995). In this study, extremely high DBT levels point to a highly anoxic reducing environment (Fig. 9b). Additionally, elevated concentrations of gammacerane and *β*-carotene are typically associated with strongly reducing conditions. The geochemical behavior of Mo and U is closely linked to the redox conditions of sedimentary water as effective proxies for reconstructing paleoenvironment (Algeo and Tribovillard, 2009; Tribovillard et al., 2012). The analyzed samples plot within Cycle 1 (with some reaching Cycle 2), indicative of an anoxic environment (Fig. 11b). Moreover, the Mo_{EF} exhibits stronger enrichment compared to the U_{EF}, suggesting that the metal-oxyhydroxide particulate shuttle facilitates the transport of Mo to sediments while exerting minimal influence on U (Qiao et al., 2023; Tribovillard et al., 2012). The widespread occurrence of framboidal pyrite and locally abundant pyrite nodules further supports the presence of an anoxic environment (Song et al., 2021; Fig. 5a, c and i). The mutual inclusion of pyrite and organic matter also serves as evidence of a synergistic relationship between anoxic conditions and organic matter preservation (Fig. 5k and l).

Paleosalinity is critical aspect of lacustrine basin environments, significantly influencing the enrichment and preservation of organic matter (Liu et al., 2024). Sr and Ba exist as ionic species in ancient lake waters, eventually precipitating as refractory minerals such as celestite and barite, which become enriched in sediments (Wei and Algeo, 2020). Generally, Sr exhibits higher solubility in saline waters compared to Ba so that the Sr/Ba ratio a reliable indicator of paleosalinity (Moore et al., 2022; Paytan et al., 2007). Sr/Ba ratios of less than 1 typically signifies a freshwater or brackish environment, whereas a ratio greater than 1 indicates brackish to saline conditions (Paytan et al., 2007). The analyzed samples generally exhibit high Sr/Ba ratios, with most falling within the brackish water depositional range, suggesting elevated salinity in the lacustrine environment (Fig. 9a). It has been proposed that Sr in carbonate reservoirs may influence clay composition signals, and the Sr/Ba index is particularly reliable when CaO exceeds 5 %. (Wei and Algeo, 2020). The high CaO content in the studied samples supports the validity of this index (Table 2). The chemical behavior of B and Ga in water systems is closely related to salinity (Liu et al., 2025; McLennan, 2001). Wei and Algeo (2020) established the B/Ga ratio as an indicator, defining B/Ga < 3 as freshwater, 3–6 as brackish, and > 6 as marine or high-salinity lacustrine environments. The B/Ga ratios in the Eq^3 of the Qianjiang Depression exhibit exceptionally high values, indicating elevated paleosalinity levels in the lake during the depositional period (Fig. 9a), which is consistent with the trends revealed by the Sr/Ba ratios. Gammacerane is a useful indicator of water column stratification, often associated with high salinity in the longitudinal profile (Luo et al., 2018; Peters et al., 2005). Elevated ETR values reflect higher salinity/alkalinity conditions in the aquatic environment and serve as an indicator of the dominant role of algae in paleoproductivity (Hou et al., 2017; Qiao et al., 2024). Prominent peaks in the *m/z* 191 fragment spectra and exceptionally high Gamm/C_{30} ($\beta\alpha + \alpha\beta$) hopane ratios, with a extremely high values of ETR, point to a highly saline lacustrine environment (Fig. 7d). *β*-carotene, derived from the synthesis of *β*-daucene by salt-tolerant algae, is enriched in response to organic matter sources and the degree of reduction in the sedimentary environment, suggesting deposition in salt lake facies or highly restricted marine settings (Peters et al., 2005; Shao et al., 2024). The Eq^3 samples

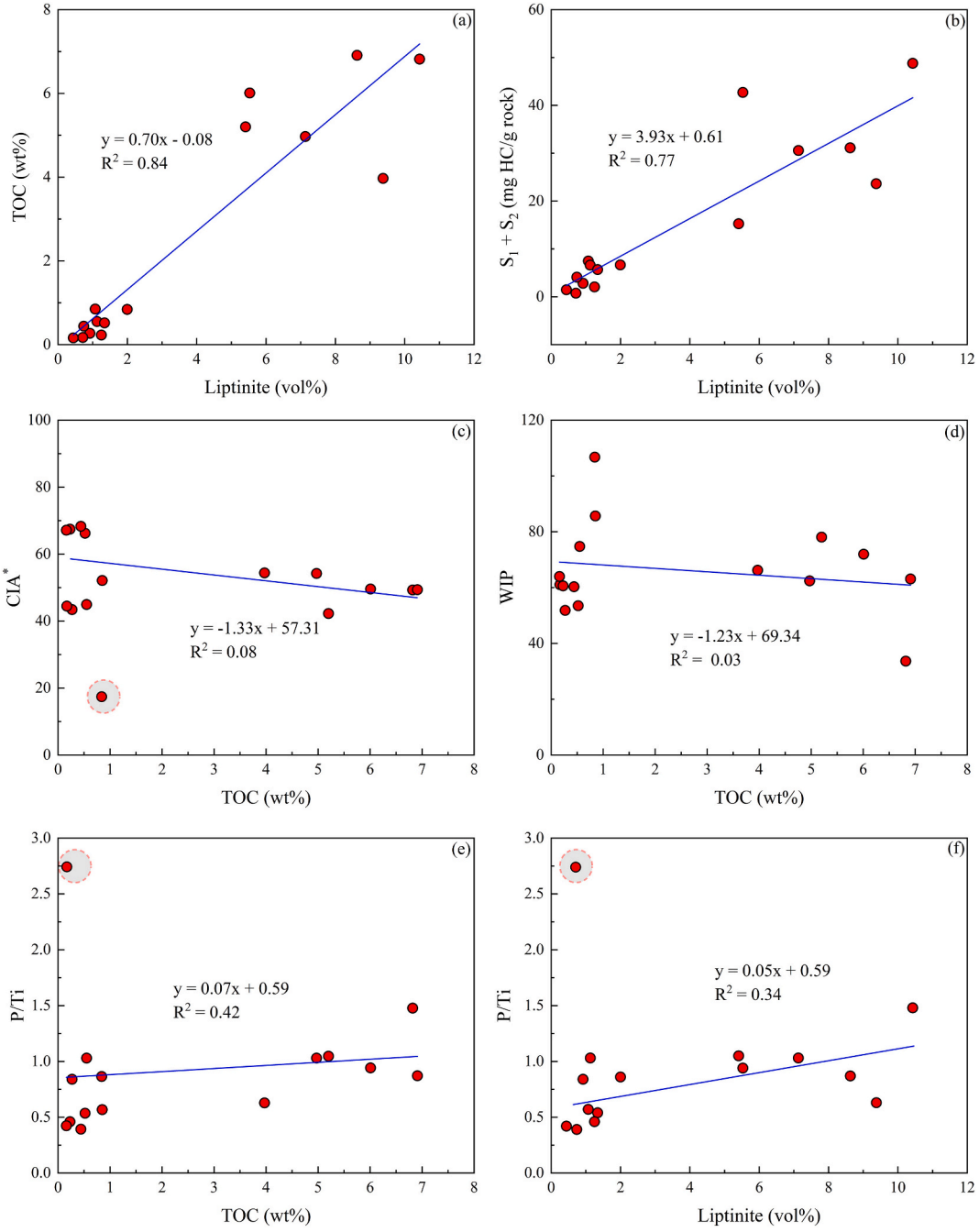

Fig. 10. Correlation scatter plots of (a) volume percentage of liptinite in organic matter versus TOC, (b) liptinite versus $S_1 + S_2$, (c) TOC versus CIA, (d) TOC versus WIP; (e) TOC versus P/Ti and (f) P/Ti versus Liptinite. The anomalous data points demarcated in the figure were systematically excluded from the linear regression analysis to preserve the statistical validity of the fitting results.

from the Tankou area exhibit abundant β-carotene, with distinct chromatographic peaks (Fig. 6a and b). The DBT/P and Pr/Ph ratios are effective tools for inferring the sedimentary environment and lithology of source rocks (Hughes et al., 1995). Majority of the studied samples plot within Zone 3 (with a few in Zone 2), indicating a hypersaline lacustrine sedimentary environment (Fig. 7b). Extremely low Pr/Ph ratios and ternary plots of DBF, F, and DBT further corroborate the hypersaline nature of the depositional environment (Peters et al., 2005; Qiao et al., 2021).

5.4. Hydrocarbon generation potential

Previous studies have consistently demonstrated that pyrolysis, maceral composition, and organic carbon content are robust methodologies for assessing the hydrocarbon generation potential of source rocks (Hou et al., 2017; Luo et al., 2017; Lei et al., 2024). In the Tankou area, the Eq^3 source rocks exhibit distinct vertical segmentation. As depth increases, the TOC content displays a declining trend, with the upper sections characterized by significantly higher TOC values compared to the lower sections (Table 1). Such elevated TOC levels are uncommon in salt lake strata but have been documented in the hydrocarbon-generating centers of the Qianjiang Depression (Hou et al., 2017). When plotted on TOC versus $S_1 + S_2$ coordinates, the upper source rocks demonstrate relatively superior quality, while the lower sections exhibit average quality, collectively indicating a favorable hydrocarbon generation potential (Fig. 2a). Notably, the majority of

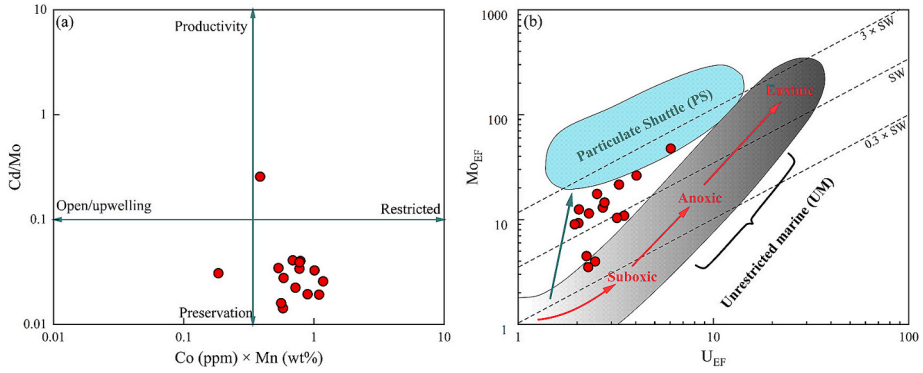

Fig. 11. (a) Co (ppm) × Mn (wt%) versus Cd/Mo (after Sweere et al., 2016); (b) U_{EF} versus Mo_{EF} (modiffed after Tribovillard et al., 2012).

samples exhibit HI exceeding 300 mg HC/g TOC. When combined with T_{max} data, these findings suggest that the source rocks in the study area predominantly contain type I-II_1 kerogen, with a minor contribution from type II_2 kerogen (Fig. 2b). The dolomitic shales within the Eq^3 interval of the Tankou slope belt are interpreted as oil-prone source rocks, enriched in oil-generating components, and share similarities with the organic matter types observed in other regions of the Qianjiang Formation within the Qianjiang Depression (Hou et al., 2017).

A comprehensive evaluation of organic matter abundance, type, and maturity is indispensable for accurately determining the hydrocarbon generation potential of source rocks. Combined with biomarker maturity parameters, the relatively low-to-medium R_o values (0.42–0.56 %) and pyrolysis T_{max} values (418–438 °C) suggest that the samples are in the immature to low-maturity level, falling short of the threshold for significant hydrocarbon expulsion according to conventional evaluation criteria (Jarvie, 2012; Misch et al., 2016; Table 1). Numerous simulation studies have proposed that the presence of salt minerals can catalyze the hydrocarbon generation process (Meng et al., 2007). This complements the previous explanation that biomarkers of maturity can reach an mature level. Within the shale samples, the proportion of liptinite exhibits a positive correlation with TOC, indicating that the high organic matter abundance in the Tankou area is closely linked to the prolific supply of algae (Fig. 10a). Furthermore, liptinite content also shows a strong positive correlation with $S_1 + S_2$, underscoring the role of algal input in enhancing the hydrocarbon generation capacity of the source rocks (Fig. 10b). Previous studies have also highlighted that high abundances of lamalginite, telalginite can facilitate the generation of immature to low-maturity oil, even at relatively low thermal maturity levels (Guo, 1993; Luo et al., 2018; Makled et al., 2021; Xie et al., 2014).

5.5. Organic matter enrichment model and influencing factors

The enrichment of organic matter in the Eq^3 interval of the Tankou slope belt within the Qianjiang Depression exhibits characteristics akin to those observed in typical saline lake basins. However, a distinctive feature of this region lies in the influence of the slope belt and the Qianbei fault, which collectively govern the composition of organic matter through terrigenous clastic input, sedimentary water conditions, and climatic factors. Based on the analysis of these influencing factors, this study establishes a comprehensive model for organic matter enrichment in continental shales within the context of a salt lake slope belt (Fig. 16). The depositional layer of the studied samples was characterized by a cold and arid climate, which played a critical role in shaping the sedimentary environment. Reduced precipitation under such conditions diminished fluvial activity, thereby limiting the influx of terrigenous debris into the basin (Morellón et al., 2009). This reduction in terrigenous input is significant, as it minimized the dilution of organic matter by the input of carbonate or clastic minerals (Ibach, 1980; Wang et al., 2022). Concurrently, the dry climate facilitated intense water evaporation, leading to elevated salinity levels in the lacustrine environment (Horsfield et al., 1994; Lu et al., 2025). High-salinity conditions promoted the stratification of the water column, creating an ideal setting for the proliferation of salt-tolerant plankton, such as algae, and establishing an anoxic environment conducive to the preservation of organic matter (Tribovillard et al., 2012; Kong et al., 2020). The stratification of the water column not only enhanced organic productivity but also restricted the diffusion of oxygen, thereby reducing the oxidation of organic material and facilitating its accumulation (Zhang et al., 2022; Wu et al., 2023). A strong positive correlation between P/Ti and TOC is observed, with P/Ti values reaching up to 2.74 at certain intervals, indicative of high primary productivity (Fig. 10e). This correlation underscores the importance of phosphate (e.g. PO_4^{3-}) as a limiting nutrient in aquatic ecosystems, driving the proliferation of phytoplankton and other aquatic organisms (Poulton, 2017; Tyrrell, 1999). The outbreak of aquatic organisms, particularly algae, played a pivotal role in enhancing organic matter productivity and enrichment. Algal blooms, fueled by nutrient availability and favorable environmental conditions, contributed significantly to the organic carbon pool, making them the primary source of organic matter in the study area (Fig. 10f). These findings underscore that terrigenous input is not a primary driver of organic

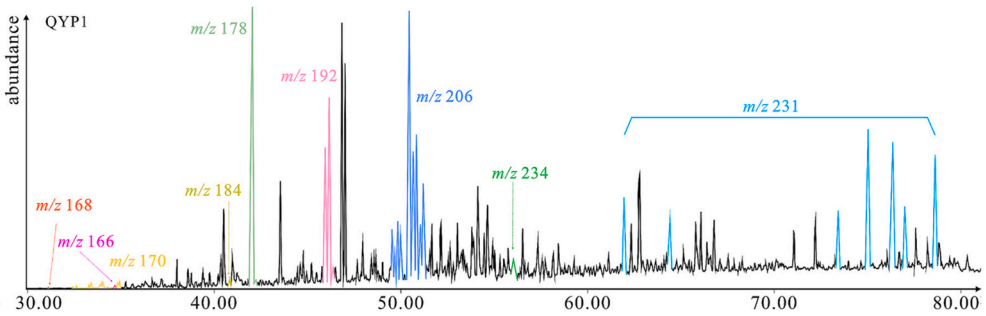

Fig. 12. Interpretation for the mass chromatogram of the main aromatic hydrocarbons used in this paper.

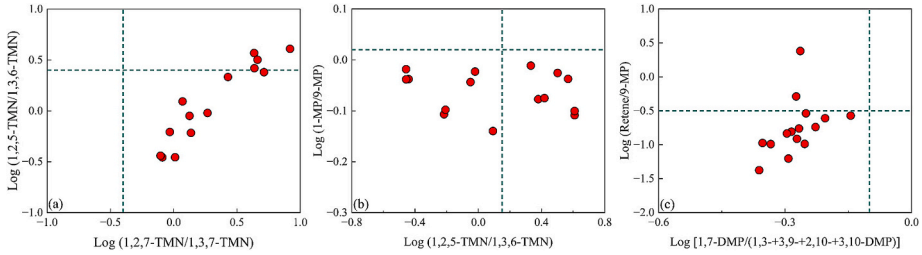

Fig. 13. Scatter diagrams of (a) log (1,2,7-TMN/1,3,7-TMN) versus log (1,2,5-TMN/1,3,6-TMN), (b) log (1,2,5-TMN/1,3,6-TMN) versus log (1-MP/9-MP) and (c) log [1,7-DMP/(1,3-+3,9-+2,10-+3,10-DMP)] versus log (Retene/9-MP), modified after Qiao et al. (2024).

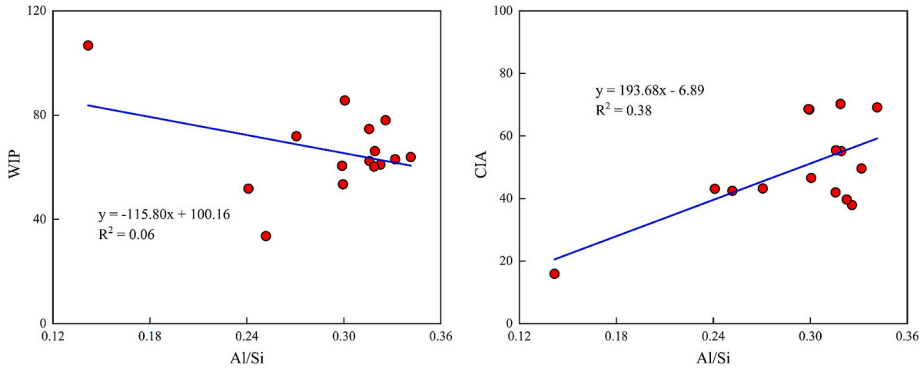

Fig. 14. Scatter plots of mol Al/Si versus (a) WIP and (b) CIA, indicating the degree of chemical weathering parameters affected by hydraulic sorting effect.

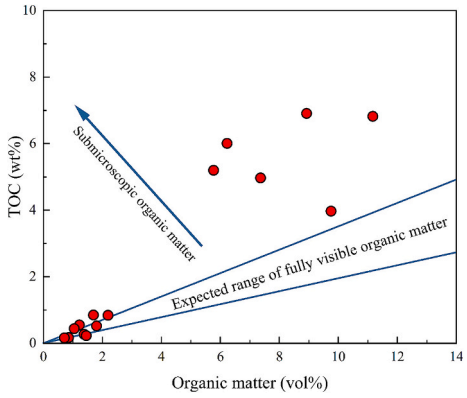

Fig. 15. The intersection graph of organic matter content versus TOC, indicating the input of relatively high submicroscopic organic matter in high TOC samples (modified after Ghassal et al., 2016).

matter enrichment in the study area. Instead, aquatic organisms, particularly algae, are the dominant contributors to organic matter accumulation (Xie et al., 2024). This geochemical evidence reinforces the notion that the study area's organic matter enrichment is primarily driven by autochthonous aquatic productivity rather than allochthonous terrigenous input. Therefore, water stratification induced by high salinity and primary paleoproductivity are the dominant factors controlling organic matter enrichment in the Eq^3 of the Qianjiang Depression. The accumulation of organic matter is also significantly influenced by preservation conditions, including strong anoxic-reducing conditions, hypersalinity with water stratification and a cold, arid climate, as evidenced by data from Co × Mn versus Cd/Mo (Fig. 11a).

Nevertheless, the Qianjiang Formation ensures a continuous supply of higher plant debris and fine-grained terrigenous material, albeit in limited quantities. The presence of higher plant debris, albeit minor, adds complexity to the organic matter composition, contributing to the heterogeneity of the source rock. In addition, due to the influence of fault activity, determining whether the deposit is in situ is crucial for identifying organic matter enrichment in the area (Wu et al., 2022b). Notably, no significant correlation is observed between TOC and CIA*, suggesting that organic matter preservation is largely unaffected by weathering processes (Fig. 10c). Consistent conclusions remain demonstrable despite the statistically insignificant linear association between TOC and WIP (Fig. 10d). This conclusion is further supported by evidence of first-cycle deposits, which confirm that the factors governing organic matter enrichment in this study are representative of the geological evolution of the basin (Fig. 4a and b). The absence of a weathering signal in the organic matter preservation highlights the dominance of original sedimentary environment controls over post-depositional alteration processes. This finding is consistent with the interpretation that the study area's organic matter enrichment is primarily driven by in situ productivity and preservation rather than external weathering influences.

6. Conclusions

The Eq^3 organic-rich sediments of Qianjiang Formation in Tankou slope belt, Qianjiang Depression, represent a promising source rock with significant hydrocarbon generation potential. The enrichment of organic matter in this unit is controlled by multiple factors, including paleoclimate, redox conditions, paleosalinity, hydrocarbon precursor input, and terrigenous clastic supply.

Low R_o and T_{max} values indicate the organic matter have reached immature to low-mature level. CPI exhibits even-carbon predominance, which tends to equilibrate with increasing depth. Biomarker parameters, including *n*-alkanes and aromatic hydrocarbons, suggest the organic-rich sediments are in the oil generation window. The organic matter abundance varies significantly, with high TOC, $S_1 + S_2$, and HI values, classifying the samples as medium to high-quality source rocks. The organic matter is predominantly type $I\text{-}II_1$ kerogen, with minor contributions from type II_2. Alginite, particularly lamalginite and telalginite, is the primary contributor to the high TOC and hydrocarbon generation potential.

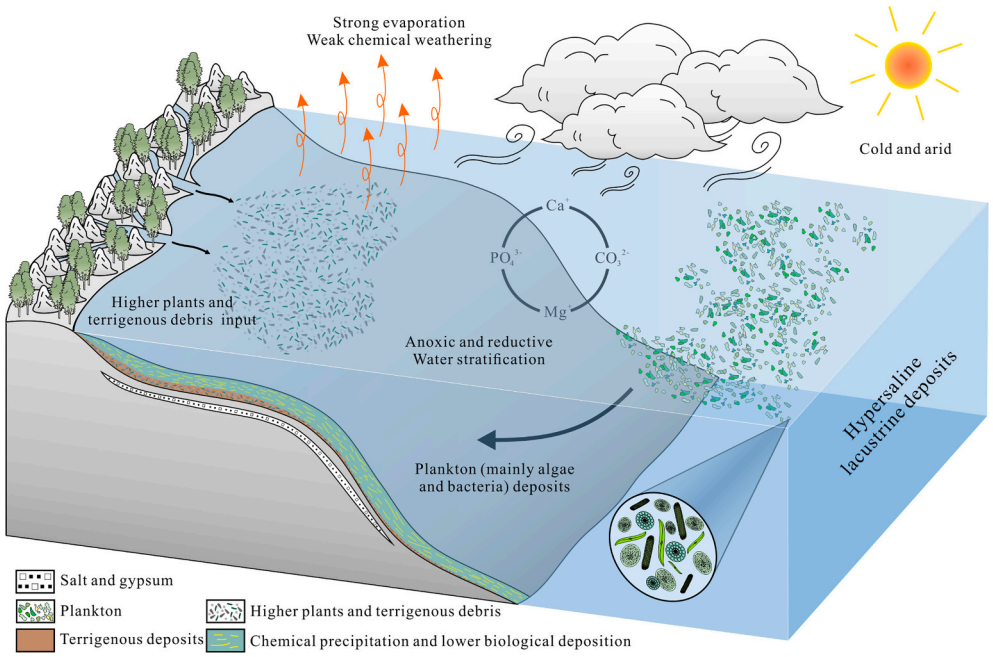

Fig. 16. Organic matter enrichment model of Eq^3 in Tankou area, Qianjiang Depression.

The Eq^3 sedimentary rocks are primarily first-cycle, iron-poor calcareous shales, enriched in CaO, MgO and Na_2O. Organic matter is dominated by lamalginite and telalginite, with minor collotelinite, telinite, and trace inertinite, suggest lower aquatic organisms constitute the principal contributors to organic matter in the Qianjiang Formation. Saturated and aromatic hydrocarbon biomarkers indicate that the hydrocarbon precursors are mainly derived from aquatic algae and salt-tolerant bacteria, with limited input from terrestrial higher plants.

Water column stratification and primary productivity serve as the principal controlling factors governing the enrichment of organic matter. Paleoclimatic conditions were cold and arid. The hypersaline, strongly reducing, and stratified water column environment is supported by biomarker and trace element indicators, including low Pr/Ph and DBT/P ratios, abundant gammacerane and β-carotane, Mo_{EF} vs. U_{EF} cross plots, and high Sr/Ba ratios. Arid climate reduced the input of terrigenous organic matter and clastics, promoting lake evaporation and high salinity. Elevated salinity facilitated water column stratification, creating favorable conditions for the proliferation of salt-tolerant algae and enhancing organic matter preservation. High P/Ti ratios indicate nutrient input that likely triggered algal blooms. The absence of chemical weathering indicates that organic matter is deposited in situ. Weak correlation between CIA and TOC suggest minimal chemical weathering, confirming that organic matter enrichment of Eq^3 in Qianjiang Depression is primarily controlled by the original depositional environment rather than post-depositional alterations.

CRediT authorship contribution statement

Rongbin Yang: Writing – original draft, Formal analysis, Data curation, Conceptualization. **Qingyong Luo:** Writing – review & editing, Resources, Funding acquisition, Conceptualization. **Jiapeng Wu:** Supervision, Investigation. **Qixiang Huang:** Validation, Formal analysis. **Man Lu:** Writing – review & editing, Visualization. **Wenxin Hu:** Investigation. **Dandan Wang:** Methodology. **Zhengyu Chen:** Methodology. **Jinqi Qiao:** Writing – review & editing.

Declaration of competing interest

We hereby confirm that all authors agreed on submission of this manuscript, that this work has not been published or submitted elsewhere, and that there aren't any other conflicts of interest.

Acknowledgments

We would like to express our gratitude to both reviewers for their constructive and insightful comments on this study. This work is supported by the National Key Research and Development Program of China (No. 2021YFA0719000) and State Key Laboratory of Petroleum Resources and Engineering, China University of Petroleum (Beijing) (No. PRE/indep-2401).

Data availability

Data will be made available on request.

References

Algeo, T.J., Tribovillard, N., 2009. Environmental analysis of paleoceanographic systems based on molybdenum-uranium covariation. Chem. Geol. 268, 211–225.
Armstroff, A., Wilkes, H., Schwarzbauer, J., Littke, R., Horsffeld, B., 2006. Aromatic hydrocarbon biomarkers in terrestrial organic matter of Devonian to Permian age. Palaeogeogr. Palaeoclimatol. Palaeoecol. 240, 253–274.
Blumenberg, M., Thiel, V., Reitner, J., 2015. Organic matter preservation in the carbonate matrix of a recent microbial mat–is there a 'mat seal effect'? Org. Geochem. 87, 25–34.
Bouchez, J., Gaillardet, J., France-Lanord, C., Maurice, L., Dutra-Maia, P., 2011. Grain size control of river suspended sediment geochemistry: clues from Amazon River depth profiles. Geochem. Geophys. Geosyst. 12, 1–24.
Brooks, D.J., Gould, K., Smith, J.W., 1969. Isoprenoid Hydrocarbons in coal and Petroleum. Nature 222, 257–259.
Budzinski, H., Garrigues, P.H., Connan, J., Devillers, J., Domine, D., Radke, M., Oudins, J.L., 1995. Alkylated phenanthrene distributions as maturity and origin indicators in crude oils and rock extracts. Geochim. Cosmochim. Acta 59, 2043–2056.
Burdige, D.J., 2007. Preservation of organic matter in marine sediments: Controls, mechanisms, and an imbalance in sediment organic carbon budgets? Chem. Rev. 107, 467–485.
Castro, A.P.D., Guedes, C.C.F., Vesely, F.F., Silveira, D.M.D., Neves, L.F., 2023. Provenance, diagenesis and reservoir quality of sandstone facies of the Maracangalha Formation, Recôncavo Basin – Northeastern Brazil. Mar. Pet. Geol. 158, 106548.
Chen, Y., Bao, J.P., Liu, Z.Q., Wang, L.Q., Deng, K., Wang, Y.P., Qi, W.Z., Gao, X.F., Jin, C.H., 2010. Relationship between rnethylphenanthrene index, methylphenanthrene ratio and organic thermal evolution: take the northern margin of Qaidam Basin as an example. Pet. Explor. Dev. 37, 508–512.

Colman, S.M., Kelts, K.R., Dinter, D.A., 2002. Depositional history and neotectonics in Great Salt Lake, Utah, from high-resolution seismic stratigraphy. Sediment. Geol. 148, 61–78.
Connan, J., Bouroullec, J., Dessort, D., Albrecht, P., 1986. The microbial input in carbonate-anhydrite facies of a sabkha palaeoenvironment from Guatemala: a molecular approach. Org. Geochem. 10, 29–50.
Cox, R.N., Lowe, D.R., Cullers, R.L., 1995. The influence of sediment recycling and basement composition on evolution of mudrock chemistry in the South-Western United States. Geochim. Cosmochim. Acta 59, 2919–2940.
Dai, S.Z., 1997. Petroleum Gology of Jianghan Saline Lacustrine Basin. Petroleum Industry Press, Beijing (in Chinese).
Davis, A., Rathbone, R.F., Lin, R., Quick, J.C., 1990. Observations concerning the nature of maceral fluorescence alteration with time. Org. Geochem. 16, 897–906.
de Souza, D.C., Carvalho, I.D., Borghi, L., Ferreira, L.D., Salgado-Campos, V.M.J., Sedorko, D., Uhlein, G.J., Araujo, B.C., 2024. Reconstructing early sedimentation patterns of the lower Codo formation (early cretaceous, NE Brazil): evidence of marine influence and the onset of an alkaline hypersaline lake. Mar. Pet. Geol. 170, 107097.
Dera, G., Pellenard, P., Neige, P., Deconinck, J.F., Puc'eat, E., Dommergues, J.L., 2009. Distribution of clay minerals in early Jurassic Peritethyan seas: palaeoclimatic signiffcance inferred from multiproxy comparisons. Palaeogeogr. Palaeoclimatol. Palaeoecol. 271, 39–51.
Doyle, C., Schroder, S., Pablo Corella, J., Valero Garces, B., 2022. Facies variability and depositional settings of Laguna Salada de Chiprana, an Iberian hypersaline lake. Sedimentology 69, 2615–2641.
Fan, P., King, J.D., Claypool, G.E., 1987. Characteristics of biomarker compounds in Chinese crude oils. In: Kumar, R.K., et al. (Eds.), Petroleum Geochemistry and Explorationin the Afro-Asian Region. Balkema, Rotterdam, pp. 197–202.
Fan, Y.C., Qi, Y.A., Dai, M.Y., Qing, G.S., Liu, B.C., Bai, W.B., 2020. Paleoclimate evolution recorded in the Cambrian Epoch 2 Zhushadong Formation from Dengfeng area, western Henan Province. J. Palaeogeogr. 22, 367–376.
Fedo, C.M., Nesbitt, H.W., Young, G.M., 1995. Unraveling the effects of potassium metasomatism in sedimentary rocks and paleosols, with implications for paleoweathering conditions and provenance. Geology 23, 921–924.
Floyd, P.A., Leveridge, B.E., 1987. Tectonic environment of the Devonian Gramscatho basin, South Cornwall: framework mode and geochemical evidence from turbiditic sandstones. J. Geol. Soc. Lond. 144, 531–542.
Garzanti, E., Padoan, M., Peruta, L., Setti, M., Najman, Y., Villa, I.M., 2013. Weathering geochemistry and Sr–Nd ffngerprints of equatorial upper Nile and Congo muds. Geochem. Geophys. Geosyst. 14, 292–316.
Ge, T.Y., Jiang, Z.X., Kong, X.X., Bao, H.Y., Chen, F.L., Wu, S.Q., Guo, L.B., Yang, Y.P., Liu, T., Zhang, J.Z., 2023. Salt rhythmite formation and organic matter enrichment in the Qianjiang formation, Jianghan Basin, China: Constraints from alternating dry and wet climates. Mar. Pet. Geol. 148, 106067.
Ghassal, B.I., Littke, R., Sachse, V., Sindern, S., Schwarzbauer, J., 2016. Depositional environment and source rock potential of Cenomanian and Turonian sedimentary rocks of the Tarfaya Basin, Southwest Morocco. Geol. Acta 14, 419–441.
Gonçalves, P.A., Kus, J., Hackley, P.C., Borrego, A.G., Hámor-Vidó, M., Kalkreuth, W., Mendonça Filho, J.G., Petersen, H.I., Pickel, W., Reinhardt, M.J., Suárez-Ruiz, I., ICCP, 2024. The petrology of dispersed organic matter in sedimentary rocks: Review and update. Int. J. Coal Geol. 294, 104604.
Gong, X.X., She, X.Y., Chen, J., Xu, H.Q., Tang, T.T., Dong, Z., 2016. The plastic deformation mechanism of Tankou salt mud uplift on the downthrow side of Qianbei fault and petroleum geological signiflcance. Chinese Journal of Geology 51, 920–933.
González-Sampériz, P., Valero-Garcés, B.L., Moreno, A., Morellón, M., Navas, A., Machín, J., Delgado-Huertas, A., 2008. Vegetation changes and hydrological fluctuations in the Central Ebro Basin (NE Spain) since the Late Glacial period:: Saline lake records. Palaeogeogr. Palaeoclimatol. Palaeoecol. 259, 157–181.
Grice, K., Schouten, S., Peters, K.E., et al., 1998. Molecular Isotopic Characterisation of Hydrocarbon Biomarkers in Palaeocene–Eocene Evaporitic, Lacustrine Source Rocks from the Jianghan Basin, China. Org. Geochem. 29, 1745–1764.
Grimalt, J., Albaiges, J., 1987. Sources and occurrence of C_{12}-C_{22} n-alkane distributions with even carbon-number preference in sedimentary environments. Geochim. Cosmochim. Acta 51, 1379–1384.
Guo, Q.J., 1993. Macerals reconsideration in the studies of "oil from coal". Pet. Explor. Dev. 2, 37–40.
Hackley, P.C., Martinez, M., 2007. Organic petrology of Paleocene Marcelina Formation coals, Paso Diablo mine, western Venezuela: Tectonic controls on coal type. Int. J. Coal Geol. 71, 505–526.
Hanson, A.D., Ritts, B.D., Zinniker, D., Moldowan, J.M., Biffi, U., 2001. Upper Oligocene lacustrine source rocks and petroleum systems of the northern Qaidam basin, Northwest China. AAPG Bull. 85, 601–619.
Holba, A.G., Ellis, L., Dzou, I.L., Hallam, A., Masterson, W.D., Francu, J., Fincannon, A.L., 2001. Extended tricyclic terpanes as age discriminators between Triassic, EarlyJurassic, and Middle-Late Jurassic oils. In: (abs.) 20th International Meeting on Organic Geochemistry, Nancy-France, 1, p. 464.
Horsfield, B., Douglas, A.G., 1980. The infuence of minerals on the pyrolysis of kerogens. Geochim. Cosmochim. Acta 44, 1119–1113.
Horsfield, B., Curry, D.J., Bohacs, K., Littke, R., RullköTter, J., Schenk, H.J., Radke, M., Schaefer, R.G., Carroll, A.R., Isaksen, G., 1994. Organic geochemistry of freshwater and alkaline lacustrine sediments in the Green River Formation of the Washakie Basin, Wyoming, U.S.A. Org. Geochem. 22, 415–440.
Hou, Y.G., Wang, F.R., He, S., Dong, T., Wu, S.Q., 2017. Properties and shale oil potential of saline lacustrine shales in the Qianjiang Depression, Jianghan Basin, China. Mar. Pet. Geol. 86, 1173–1190.
Hower, C.J., Trinkle, E.J., Raione, R.P., 2008. Vickers microhardness of telovitrinite and pseudovitrinite from high volatile bituminous Kentucky coals. Int. J. Coal Geol. 75, 76–80.
Huang, C.J., Hinnov, L., 2014. Evolution of an Eocene-Oligocene saline lake depositional system and its controlling factors, Jianghan Basin, China. J. Earth Sci. 25, 959–976.
Huang, C.J., Hinnov, L., 2019. Astronomically forced climate evolution in a saline lake record of the middle Eocene to Oligocene, Jianghan Basin, China. Earth Planet. Sci. Lett. 528, 115946.
Hubert, H.L., Rankey, E.C., Omelon, C., 2018. Organic matter, textures and pore attributes of hypersaline microbial deposits (Holocene, Bahamas). J. Sediment. Res. 88, 827–849.
Hughes, W.B., Holba, A.G., Dzou, L.I., 1995. The ratios of dibenzothiophene to phenanthrene and pristane to phytane as indicators of depositional environment and lithology of petroleum source rocks. Geochim. Cosmochim. Acta 59, 3581–3598.
Hutton, A.C., Hower, J.C., 1999. Cannel coals: implications for classification and terminology. Int. J. Coal Geol. 41, 157–188.
Ibach, L.E.J., 1980. Relationship between sedimentation rate and total organic carbon content in ancient marine sediments. AAPG Bull. 66, 170–188.
International Committee for Coal and Organic Petrology (ICCP), 1998. The new vitrinite classification (ICCP System 1994). Fuel 77, 349–358.
ISO 7404–5, 2009. Methods for the Petrographic Analysis of Coal—Part 5: Methods of Determining Microscopically the Reffectance of Vitrinite. International Organization for Standardization, Geneva, Switzerland, p. 14.
Jarvie, D.M., 2012. Shale resource systems for oil and gas: part 1–Shale-gasresource systems. In: Breyer, J.A. (Ed.), Shale Reservoirs–Giant Resources for the 21st Century, AAPG Memoir, 97. The AAPG, pp. 69–87.
Jarvie, D.M., Hill, R.J., Ruble, T.E., Pollastro, R.M., 2007. Unconventional shale-gas systems: the Mississippian Barnett Shale of north-Central Texas as one model for thermogenic shale-gas assessment. AAPG Bull. 91, 475–499.
Jeng, W.L., Huh, C.A., 2008. A comparison of sedimentary aliphatic hydrocarbon distribution between East China Sea and southern Okinawa Trough. Cont. Shelf Res. 28, 582–592.
Ji, C.J., Yi, H.S., Xia, G.Q., Chen, Y., Wu, C.H., Mao, L.L., Cai, Z.H., Li, Q.L., 2014. Geochemical characteristics and significance of aromatic hydrocarbon of Long'eni area crude oil in Qiangtang Basin. Acta Sedimentol. Sin. 32, 391–398.
Johns, W.D., Shimoyama, A., 1972. Clay minerals and petroleum forming reaction durial an diagenesis. AAPG Bull. 56, 2160–2167.
Khan, W., Zhang, K., Liang, H., Yu, P., 2023. Provenance for the Makran Flysch Basin in Pakistan: Implications for interaction between the Indian, Eurasian, and Arabian plates. J. Asian Earth Sci. 248, 105626.
Kolaczkowska, E., 1990. Thermodynamic stability of various alkylated, dealkylated and rearranged 17α- and 17β-hopane isomers using molecular mechanics calculations. Org. Geochem. 16, 1033–1038.
Kong, X.X., Jiang, Z.X., Zheng, Y.H., Xiao, M., Chen, C., Yuan, H., Chen, F.L., Wu, S.Q., Zhang, J.G., Han, C., Liu, S.Q., 2020. Organic geochemical characteristics and organic matter enrichment of mudstones in an Eocene saline lake, Qianjiang Depression, Hubei Province, China. Mar. Pet. Geol. 114, 104194.
Kong, X.X., Jiang, Z.X., Ju, B.S., Liang, C., Cai, Y., Wu, S.Q., 2022. Fine-grained carbonate formation and organic matter enrichment in an Eocene saline rift lake (Qianjiang Depression): Constraints from depositional environment and material source. Mar. Pet. Geol. 138, 105534.
Köster, J., van Kaam-Peters, H.M.E., Koopmans, M.P., de Leeuw, J.W., Sinninghe Damsté, J.S., 1997. Sulphurisation of homohopanoids: Effects on carbon number distribution, speciation, and 22S/22R epimer ratios. Geochim. Cosmochim. Acta 61, 2431–2452.
Kus, J., Araujo, C.V., Borrego, A.G., Flores, D., Hackley, P.C., Hámor-Vidó, M., Kalaitzidis, S., Kommeren, C.J., Kwiecińska, B., Mastalerz, M., Mendonça Filho, J.G., Menezes, T.R., Misz-Kennan, M., Nowak, G.J., Petersen, H.I., Rallakis, D., Suárez-Ruiz, I., Sýkorova, I., Životić, D., 2017. Identification of alginite and bituminite in rocks other than coal. 2006, 2009, and 2011 round robin exercises of the ICCP Identification of Dispersed Organic Matter Working Group. Int. J. Coal Geol. 178, 26–38.
Kvalheim, O.M., Christy, A.A., TelnæS, N., BjøRseth, A., 1987. Maturity determination of organic matter in coals using the methylphenanthrene distribution. Geochim. Cosmochim. Acta 51, 1883–1888.
Lee, C., Love, G.D., Jahnke, L.L., Kubo, M.D., Des Marais, D.J., 2019. Early diagenetic sequestration of microbial mat lipid biomarkers through covalent binding into insoluble macromolecular organic matter (IMOM) as revealed by sequential chemolysis and catalytic hydropyrolysis. Org. Geochem. 132, 11–22.
Lei, C., Yin, S.Y., Ye, J.R., Wu, J.F., Wang, Z.S., Gao, Bin, 2024. Geochemical Characteristics and Hydrocarbon Generation Modeling of the Paleocene Source Rocks in the Jiaojiang Sag, East China Sea Basin. J. Earth Sci. 35, 642–654.
Liu, B., Bechtel, A., Gross, D., Fu, X.F., Li, X.N., Sachsenhofer, R.F., 2018. Middle Permian environmental changes and shale oil potential evidenced by high-resolution organic petrology, geochemistry and mineral composition of the sediments in the Santanghu Basin, Northwest China. Int. J. Coal Geol. 185, 119–137.
Liu, S.J., Gao, G., Jin, J., Gang, W.Z., Xiang, B.L., 2022. Source rock with high abundance of C28 regular sterane in typical brackish-saline lacustrine sediments: Biogenic source, depositional environment and hydrocarbon generation potential in Junggar Basin, China. J. Pet. Sci. Eng. 208, 109670.
Liu, B., Wang, L., Fu, X.F., Huo, Q.L., Bai, L.H., Lyu, J.C., Wang, B.Y., 2023a. Identification, evolution and geological indications of solid bitumen in shales: a case study of the first member of cretaceous Qingshankou Formation in Songliao Basin, NE China. Pet. Explor. Dev. 50, 1345–1357.
Liu, S.M., Jiang, L., Liu, B.J., Zhao, C.L., Tang, S.H., Tan, F.R., 2023b. Investigation of Organic Matter sources and Depositional Environment changes for Terrestrial Shale

Succession from the Yuka Depression: Implications from Organic Geochemistry and Petrological analyses. J. Earth Sci. 34, 1577–1595.
Liu, Q.H., Li, Z.Y., Chen, H.H., Zhou, Z.Q., Tan, M.X., Zhu, X.M., 2024. Current Geological Issues and Future Perspectives in Deep-Time Source-to-Sink Systems of Continental Rift Basins. J. Earth Sci. 35, 1758–1764.
Liu, Z.H., Algeo, T.J., Brocks, J.J., van Maldegem, L.M., Gilleaudeau, G.J., Kah, L.C., Cheng, M., Yu, W.C., 2025. Salinity reconstruction in Proterozoic depositional systems. Geol. Soc. Am. Bull. 137, 447–464.
Lu, M., Duan, G.Q., Zhang, T.X., Liu, N.H., Song, Y.X., Zhang, Z.Z., Qiao, J.Q., Wang, Z. Y., Fang, Z.L., Luo, Q.Y., 2025. Influences of paleoclimatic changes on organic matter enrichment mechanisms in freshwater and saline lacustrine oil shales in China: a machine learning approach. Earth Sci. Rev. 262, 105061.
Luo, Q.Y., Qu, Y.S., Chen, Q., Xiong, Z.R., 2017. Organic geochemistry and petrology of mudrocks from the upper Carboniferous Batamayineishan Formation, Wulungu Area, Junggar Basin, China: Implications for petroleum exploration. Energy Fuel 31, 10628–10638.
Luo, Q.Y., Gong, L., Qu, Y.S., Zhang, K.H., Zhang, G.L., Wang, S.Z., 2018. The tight oil potential of the Lucaogou Formation from the southern Junggar Basin, China. Fuel 234, 858–871.
Lupker, M., France-Lanord, C., Galy, V., Lave, J., Gaillardet, J., Gajurel, A.P., Guilmette, C., Rahman, M., Singh, S.K., Sinha, R., 2012. Predominant floodplain over mountain weathering of Himalayan sediments (Ganga basin). Geochim. Cosmochim. Acta 84, 410–432.
Mackenzie, A.S., Patience, R.L., Maxwell, J.R., Vandenbroucke, M., Durand, B., 1980. Molecular parameters of maturation in the Toarcian shales, Paris Basin, France—I. Changes in the configurations of acyclic isoprenoid alkanes, steranes and triterpanes. Geochim. Cosmochim. Acta 44, 1709–1721.
Makled, W.A., Farouk, S., Al-Hadidy, A.H., Mohammed, I.Q., Fadhil, A.L., 2021. Organic petrography of Ordovician-Silurian rocks and their implications to hydrocarbon generation in the Akkas-1 well, western Iraq: New evidence for the Ordovician Gloeocapsomorpha and glaciation events. Mar. Pet. Geol. 128, 105053.
McLennan, S.M., 1993. Weathering and global denudation. J. Geol. 101, 295–303.
McLennan, S.M., 2001. Relationships between the trace element composition of sedimentary rocks and upper continental crust. Geochem. Geophys. Geosyst. 2.
Mclennan, S.M., Taylor, S.R., Mcculloch, M.T., Maynard, J.B., 1990. Geochemical and Nd-Sr isotopic composition of deep-sea turbidites: Crustal evolution and plate tectonic associations. Geochim. Cosmochim. Acta 54, 2015–2050.
Meng, Q.X., Sun, M.Z., Fang, X., Wang, Z.D., Wang, G.C., Xu, Y., 2007. Hydrocarbon generation mechanism and evolution characteristics of biomarkers on low-evolutionary source rocks of the salt lacustrine facies. Acta Sedimentol. Sin. 25, 800–807.
Misch, D., Gross, D., Mahlstedt, N., Makogon, V., Sachsenhofer, R.F., 2016. Shale gas/shale oil potential of Upper Visean Black Shales in the Dniepr-Donets Basin (Ukraine). Mar. Pet. Geol. 75, 203–219.
Moldowan, J.M., Seifert, W.K., Gallegos, E.J., 1985. Relationship between petroleum composition and depositional environment of petroleum source rocks. AAPG Bull. 69, 1255–1268.
Moore, T.A., Dai, S.F., Huguet, C., Pearse, J., Liu, J.J., Esterle, J.S., Jia, R.K., 2022. Petrographic and geochemical characteristics of selected coal seams from the late Cretaceous-Paleocene Guaduas Formation, Eastern Cordillera Basin, Colombia. Int. J. Coal Geol. 259, 104042.
Morellón, M., Valero-Garcés, B., Vegas-Vilarrúbia, T., González-Sampériz, P., Romero, Ó., Delgado-Huertas, A., Mata, P., Moreno, A., Rico, M., Corella, J.P., 2009. Late glacial and Holocene palaeohydrology in the western Mediterranean region: the Lake Estanya record (NE Spain). Quat. Sci. Rev. 28, 2582–2599.
Morton, A.C., Chisholm, J.I., Frei, D., 2024. Provenance response to evolving palaeogeography recorded by Carboniferous sandstones in the northern Pennine Basin, UK. Sediment. Geol. 470, 106691.
Mukherjee, S., Rajabi, M., Esterle, J., 2021. Relationship between coal composition, fracture abundance and initial reservoir permeability: a case study in the Walloon Coal measures, Surat Basin, Australia. Int. J. Coal Geol. 240, 103726.
Nesbitt, H., Young, G.M., 1982. Early Proterozoic climates and plate motions inferred from major element chemistry of lutites. Nature 299, 715–717.
Nunn, J.A., Harris, N.B., 2007. Subsurface seepage of seawater across a barrier: a source of water and salt to peripheral salt basins. Geol. Soc. Am. Bull. 119, 1201–1217.
Ottenjann, K., 1988. Fluorescence alteration and its value for studies of maturation and bituminization. Org. Geochem. 12, 309–321.
Pakdel, H., Roy, C., Kalkreuth, W., 1999. Oil production by vacuum pyrolysis of Canadian oil shales and fate of the biological markers. Fuel 78, 365–375.
Parker, A., 1970. An Index of Weathering for Silicate Rocks. Geol. Mag. 107, 501–504.
Paytan, A., Averyt, K., Faul, K., Gray, E., Thomas, E., 2007. Barite accumulation, ocean productivity, and Sr/Ba in barite across the Paleocene-Eocene thermal Maximum. Geology 35, 1139–1142.
Peakman, T.M., ten Haven, H.L., de Leeuw, J.W., Rechka, J.R., Maxwell, J.R., 1989. Occurrence of (20R)- and (20S)- Δ8(14) and Δ14 5α (H)-sterenes and the origin of 5α (H),14β(H),17β (H)-steranes in an immature sediment. Geochim. Cosmochim. Acta 53, 2001–2009.
Peters, K.E., Cassa, M.R., 1994. Applied source rock geochemistry. In: Magoon, L.B., Dow, W.G. (Eds.), The Petroleum System—From Source to Trap, vol. 60. AAPG Memoir, pp. 93–117.
Peters, K.E., Walters, C.C., Moldowan, J.M., 2005. The Biomarker Guide, v. 2: Biomarkersand Isotopes in Petroleum Exploration and Earth history. Cambridge UniversityPress, Cambridge, pp. 5–209.
Philp, R.P., Li, J., Lewis, C.A., 1989. An Organic Geochemical Investigation of crude oils from Shanganning, Jianghan, Chaidamu and Zhungeer Basins, People's Republic of China. Org. Geochem. 14, 447–460.
Pichevin, L., Bertrand, P., Boussafir, M., Disnar, J., 2004. Organic matter accumulation and preservation controls in a deep sea modern environment: an example from Namibian slope sediments. Org. Geochem. 35, 543–559.
Pickel, W., Kus, J., Flores, D., Kalaitzidis, S., Christanis, K., Cardott, B.J., Misz-Kennan, M., Rodrigues, S., Hentschel, A., Hamor-Vido, M., Crosdale, P., Wagner, N., ICCP, 2017. Classification of liptinite – ICCP System 1994. Int. J. Coal Geol. 169, 40–61.
Pilcher, R.S., Blumstein, R.D., 2007. Brine volume and salt dissolution rates in Orca Basin Northeast Gulf of Mexico. AAPG Bull. 91, 823–833.
Poulton, S.W., 2017. Biogeochemistry: early phosphorus redigested. Nat. Geosci. 10, 75–76.
Powell, T.G., Mckirdy, D.M., 1973. Relationship between ratio of pristane to phytane, crude oil composition and geological environment in Australia. Nature 243, 37–39.
Pu, X.G., Qi, Z.X., Zheng, X.L., Han, D.X., 2002. Basic petroleum geological characteristics and resource potential of inter-salt non-sandstone reservoir. Pet. Explor. Dev. 29 (28–30), 36.
Püttmann, W., Villar, H., 1987. Occurrence and geochemical significance of 1,2,5,6-tetramethylnaphthalene. Geochim. Cosmochim. Acta 51, 3023–3029.
Qiao, J.Q., Grohmann, S., Baniasad, A., Zhang, C., Jiang, Z.X., Littke, R., 2021. High microbial gas potential of Pleistocene lacustrine deposits in the central Qaidam Basin, China: an organic geochemical and petrographic assessment. Int. J. Coal Geol. 245, 103818.
Qiao, J.Q., Littke, R., Grohmann, S., Zhang, C., Jiang, Z.X., Strauss, H., Zieger, L., 2022. Climatic and environmental conditions during the Pleistocene in the Central Qaidam Basin, NE Tibetan Plateau: evidence from GDGTs, stable isotopes and major and trace elements of the Qigequan Formation. Int. J. Coal Geol. 254, 103958.
Qiao, J.Q., Luo, Q.Y., Zhang, K.H., Zhang, G.L., Duan, J.C., Wang, D.D., Yu, H.Z., Wang, S.Z., Qu, Y.S., Kopaevich, L., 2023. Geochemistry and organic petrography of the Middle Permian Lucaogou alkaline lacustrine oil shale in the southern Junggar Basin, China: Implications for formation conditions and organic matter accumulation. Int. J. Coal Geol. 268, 104198.
Qiao, J.Q., Luo, Q.Y., Guo, S.X., Tang, X.L., Kopaevich, L., Littke, R., 2024. Organic petrology andgeochemistry of the late Neogene Shizigou Formation in the Qaidam Basin, China: characteristics of a prospective microbial gas source rock. Int. J. Coal Geol. 296, 104658.
Qiao, J.Q., Luo, Q.Y., Tang, X.L., Wang, D.D., Kopaevich, L., Khan, I., 2025. Geochemistry and mineralogy of the late Neogene alkaline megalake sediments in the Qaidam Basin (China): Implications for provenance, tectonics, paleoclimate, paleoenvironment and organic matter accumulation. Appl. Geochem. 183, 106339.
Romero-Viana, L., Kienel, U., Sachse, D., 2012. Lipid biomarker signatures in a hypersaline lake on Isabel Island (Eastern Paciffc) as a proxy for past rainfall anomaly (1942–2006 AD). Palaeogeogr. Palaeoclimatol. Palaeoecol. 350, 49–61.
Rullkötter, J., Marzi, R., 1988. Natural and artificial maturation of biological markers in a Toarcian shale from northern Germany. Org. Geochem. 13, 639–645.
Rullkötter, J., Spiro, B., Nissenbaum, A., 1985. Biological marker characteristics of oils and asphalts from carbonate source rocks in a rapidly subsiding graben, Dead Sea, Israel. Geochim. Cosmochim. Acta 49, 1357–1370.
Sachsenhofer, R.F., Gratzer, R., Tschelaut, W., Bechtel, A., 2006. Characterisation of non-producible oil in Eocene reservoir sandstones (Bad Hall Nord field, Alpine Foreland Basin, Austria). Mar. Pet. Geol. 23, 1–15.
Salah, M.K.K., Janjuhah, H.T., Sanjuan, J., 2023. Analysis and Characterization of Pore System and Grain Sizes of Carbonate Rocks from Southern Lebanon. J. Earth Sci. 34, 101–121.
Scott, A.C., 2002. Coal petrology and the origin of coal macerals: a way ahead? Int. J. Coal Geol. 50, 119–134.
Seifert, W.K., Moldowan, J.M., 1978. Applications of steranes, terpanes and monoaromatics to the maturation, migration and source of crude oils. Geochim. Cosmochim. Acta 42, 77–95.
Shao, M., Lei, T.Z., Zhang, S.C., Zhang, S.Y., Pei, Y., Song, S., 2024. Effects of Volcanic activity on Organic Matter sources and the Paleoenvironment: Geochemical evidence from Upper Carboniferous Source Rocks (Batamayineishan Formation) in Eastern Junggar, NW China. J. Earth Sci. 35, 1482–1498.
Shi, S.Y., Hu, S.Y., Liu, W., Wang, T.S., Zhou, G., Xu, A.N., Huang, Q.Y., Xu, Z.H., Hao, B., Wang, K., Jiang, H., Ma, K., Bai, Z.Z., 2024. Hydrocarbon accumulation in deep ancient carbonate-evaporite assemblages. Pet. Explor. Dev. 51, 54–68.
Sinninghe Damsté, J.S., Kenig, F., Koopmans, M.P., Köster, J., Schouten, S., Hayes, J.M., de Leeuw, J.W., 1995. Evidence for gammacerane as an indicator of water column stratification. Geochim. Cosmochim. Acta 59, 1895–1900.
Song, L.S., Bhattacharya, S., Webb, Z., Fowler, A., Lee, V., 2021. Preservation of organic carbon in the cretaceous Hue Shale on the North Slope of Alaska: Insights from pyrite morphology. Int. J. Coal Geol. 235, 103678.
Suárez-Ruiz, I., Flores, D., Mendonça Filho, J.G., Hackley, P.C., 2012. Review and update of the applications of organic petrology: part 1, geological applications. Int. J. Coal Geol. 99, 54–112.
Suttner, L.J., Dutta, P.K., 1986. Alluvial sandstone composition and paleoclimate; I, framework mineralogy. J. Sediment. Res. 56, 329–345.
Suttner, L.J., Basu, A., Mack, G.H., 1981. Climate and the origin of quartz arenites. J. Sediment. Res. 51, 1235–1246.
Sweere, T., van den Boorn, S., Dickson, A.J., Reichart, G.J., 2016. Deffnition of new trace metal proxies for the controls on organic matter enrichment in marine sediments based on Mn, Co, Mo and Cd concentrations. Chem. Geol. 441, 235–245.
Synnott, D.P., Dewing, K., Ardakani, O.H., Schwark, L., Percy, E.L., Pedersen, P.K., 2023. Comparison of optical and geochemical thermal maturity parameters over a stratigraphically controlled natural transect. Mar. Pet. Geol. 154, 106332.

Szczerba, M., Rospondek, M.J., 2010. Controls on distributions of methylphenanthrenes in sedimentary rock extracts: critical evaluation of existing geochemical data from molecular modelling. Org. Geochem. 41, 1297–1311.
Taylor, S.R., McLennan, S.M., 1985. The Continental Crust: Its Composition and Evolution. Blackwell, Oxford, p. 312.
Thompson-Butler, William, Peters, K.E., Magoon, L.B., Scheirer, A.H., Moldowan, J.M., Blanco, V.O., Blanco, Vladimir Orlando, Gonzalez, R.E., Graham, S.A., Zumberge, J. E., Wavrek, D.A., et al., 2019. Identiffcation of genetically distinct petroleum tribes in the Middle Magdalena Valley, Colombia. AAPG Bull. 103, 3003–3034.
Tribovillard, N., Algeo, T.J., Lyons, T., Riboulleau, A., 2006. Trace metals as paleoredox and paleoproductivity proxies: an update. Chem. Geol. 232, 12–32.
Tribovillard, N., Algeo, T.J., Baudin, F., Riboulleau, A., 2012. Analysis of marine environmental conditions based on molybdenum-uranium covariation-applications to Mesozoic paleoceanography. Chem. Geol. 324, 46–58.
Tyrrell, T., 1999. The relative influences of nitrogen and phosphorus on oceanic primary production. Nature 400, 525–531.
van Aarssen, B., Alexander, R., Kagi, R.I., 2000. Higher plant biomarkers reffect palaeovegetation changes during Jurassic times. Geochim. Cosmochim. Acta 64, 1417–1424.
Volkman, J.K., Zhang, Z., Xie, X., Qin, J., Borjigin, T., 2015. Biomarker evidence for Botryococcus and a methane cycle in the Eocene Huadian oil shale, NE China. Org. Geochem. 78, 121–134.
Walczak, A., Belka, Z., 2017. Fingerprinting Gondwana versus Baltica provenance: Nd and Sr isotopes in lower Paleozoic clastic rocks of the Małopolska and Łysogóry terranes, southern Poland. Gondwana Res. 45, 138–151.
Wang, E.Z., Guo, T.L., Liu, B., Li, M.W., Xiong, L., Dong, X.X., Zhang, N.X., Wang, T., 2022. Lithofacies and pore features of marine-continental transitional shale and gas enrichment conditions of favorable lithofacies: A case study of Permian Longtan Formation in the Lintanchang area,southeast of Sichuan Basin, SW China. Pet. Explor. Dev. 49, 1132–1142.
Wang, Z.C., Xin, Y.G., Xie, W.R., Wen, L., Zhang, H., Xie, Z.Y., Zhang, J.Y., Tian, H., Li, W.Z., Fu, X.D., Sun, H.F., Wang, X.F., Hu, G.Y., Zhang, Y., 2023. Petroleum geology of marl in Triassic Leikoupo Formation and discovery significance of well Chongtan-1 in Central Sichuan Basin, SW China. Pet. Explor. Dev. 50, 950–961.
Waples, D.W., Machihara, T., 1991. Biomarkers for geologists, a practical guide to the application of steranes and triterpanes in petroleum geology. In: Methods in Exploration Series 9. AAPG, Tulsa Oklahoma.
Warren, J.K., 2006. Evaporites: Sediments, Resources, and Hydrocarbons. Springer, Berlin, New York, p. 1035.
Wehner, H., Teschner, M., Bosecker, K., 1986. Chemical reactions and stability of biomarkers and stable isotope ratios during in vitro biodegradation of petroleum. Org. Geochem. 10, 463–471.
Wei, W., Algeo, T.J., 2020. Elemental proxies for paleosalinity analysis of ancient shales and mudrocks. Geochim. Cosmochim. Acta 287, 341–366.
Wu, Z.R., Grohmann, S., Littke, R., Guo, T.X., He, S., Baniasad, A., 2022a. Organic petrologic and geochemical characterization of petroleum source rocks in the Middle Jurassic Dameigou Formation, Qaidam Basin, northwestern China: Insights into paleo-depositional environment and organic matter accumulation. Int. J. Coal Geol. 259, 104038.
Wu, Z.R., He, S., He, Z.L., Li, X.C., Zhai, G.Y., Huang, Z.Q., 2022b. Petrographical and geochemical characterization of the Upper Permian Longtan formation and Dalong Formation in the lower Yangtze region, South China: Implications for provenance, paleoclimate, paleoenvironment and organic matter accumulation mechanisms. Mar. Pet. Geol. 139, 105580.
Wu, Z.R., Littke, R., Baniasad, A., Yang, Z., Tang, Z.X., Grohmann, S., 2023. Geochemistry and petrology of petroleum source rocks in the Upper cretaceous Qingshankou Formation, Songliao Basin, NE China. Int. J. Coal Geol. 270, 104222.
Wu, Z.R., Grohmann, S., Littke, R., 2024. Geochemistry and petrology of early Permian lacustrine shales in the Lodève Basin, Southern France: Depositional history, organic matter accumulation and thermal maturity. Int. J. Coal Geol. 284, 10446.
Xiao, X.M., Wilkins, R.W.T., Liu, D.H., Liu, Z.F., Shen, J.Q., 2002. Laser-induced fluorescence microscopy - application to possible high rank and carbonate source rocks. Int. J. Coal Geol. 51, 129–141.
Xie, X.M., Volkman, J.K., Qin, J.Z., Borjigin, T., Bian, L.Z., Zhen, L.J., 2014. Petrology and hydrocarbon potential of microalgal and macroalgal dominated oil shales from the Eocene Huadian Formation, NE China. Int. J. Coal Geol. 124, 36–47.
Xie, H.Y., Jiang, Z.X., Wang, L., Xue, X.Y., 2024. Organic matter enrichment model of fine-grained rocks in volcanic rift lacustrine basin: a case study of lower submember of second member of lower cretaceous Shahezi Formation in Lishu rift depression of Songliao Basin, NE China. Pet. Explor. Dev. 51, 1232–1246.
Xu, X.T., Shao, L.Y., 2018. Limiting factors in utilization of chemical index of alteration of mudstones to quantify the degree of weathering in provenance. J. Palaeogeogr. 20, 515–522.
Yu, M., Gao, G., Liu, M., Liang, H., Kang, J.L., Xu, X.F., Zhao, X.Y., 2024. Sedimentary environment shift and organic matter enrichment mechanism in response to volcanic ash influence: a case study of the Permian Lucaogou Formation, Santanghu Basin, NW China. J. Palaeogeogr. 13, 793–822.
Zhang, M., Philp, P., 2010. Geochemical characterization of aromatic hydrocarbons in crude oils from the Tarim, Qaidam and Turpan Basins, NW China. Pet. Sci. 7, 448–457.
Zhang, K., Song, Y., Jia, C.Z., Jiang, Z.X., Han, F.L., Wang, P.F., Yuan, X.J., Yang, Y.M., Zeng, Y., Li, Y., Li, Z.W., Liu, P., Tang, L.Y., 2022. Formation mechanism of the sealing capacity of the roof and floor strata of marine organic-rich shale and shale itself, and its influence on the characteristics of shale gas and organic matter pore development. Mar. Pet. Geol. 140, 105647.